Radiative decay of the resonant K^* and the $\gamma K \to K\pi$ amplitude from lattice QCD

Archana Radhakrishnan[1,2,*] Jozef J. Dudek[1,2,†] and Robert G. Edwards[2,‡]

(for the Hadron Spectrum Collaboration)

[1]*Department of Physics, College of William and Mary, Williamsburg, Virginia 23187, USA*
[2]*Thomas Jefferson National Accelerator Facility, 12000 Jefferson Avenue,*
Newport News, Virginia 23606, USA

We present the first calculation in lattice QCD of the process $\gamma K \to K\pi$ in which the narrow K^* vector resonance appears. Using a lattice on which the pion has a mass of 284 MeV, we determine the transition amplitude at 128 points in the $(Q^2, E_{K\pi})$ plane, and find suitable resonant scattering descriptions. We demonstrate the need to account for S-wave $K\pi$ elastic scattering when converting the finite-volume matrix elements computed in lattice QCD to the physically relevant infinite-volume matrix elements, even when we are primarily interested in the P-wave amplitude. Analytically continuing parametrizations of the $\gamma K \to K\pi$ amplitude to the K^* resonance pole, we obtain the $K^{*+} \to K^+\gamma$ transition form factor and compare the $Q^2 = 0$ value to the corresponding value extracted from the experimental partial decay width.

I. INTRODUCTION

The K^* is a well-established experimental resonance, typically observed as a narrow peak in any process leading to a $K\pi$ final state. As well as its sole hadronic decay mode to $K\pi$, the K^* also has a much weaker decay mode to $K\gamma$, and the rate for this has been determined experimentally by considering the process $\gamma K \to K\pi$. This is achieved using a kaon beam on nuclear targets, where the very small momentum transfer region is dominated by a nearly real photon exchange, in what is known as the Primakoff process. Experiments were performed with both charged and neutral (K_L^0) kaon beams in the 1970s and 1980s [1–4], yielding estimates for the partial decay widths [averaged by the particle data group (PDG)] of

$$\Gamma(K^{*\pm} \to K^\pm \gamma) = 50(5) \text{ keV},$$
$$\Gamma(K^{*0} \to K^0 \gamma) = 116(10) \text{ keV}.$$

*archana.radhakrishnan@tifr.res.in
†dudek@jlab.org
‡edwards@jlab.org

At the time of the experiments, the most sophisticated theoretical tool available to describe these numbers was the constituent quark model, and these rates were interpreted in terms of constituent-quark magnetic moments, leading to estimates of the degree of $SU(3)$ flavor symmetry breaking.

Today we would seek to understand these numbers within nonperturbative quantum chromodynamics, either directly, as we will do in this paper, using lattice QCD, or indirectly using chiral effective field theory. Dax *et al.* have emphasized the connection of these radiative processes to the chiral anomaly which is a leading effect in such an effective field theory approach [5].

In order to study this process rigorously, one should utilize theoretical techniques which respect, to the highest degree possible, the general constraints of scattering theory. A particularly important constraint in the current case is that of *unitarity*—the strong rescattering of $K\pi$ through the K^* resonance is limited by unitarity, and correct application leads to a restriction on the possible behavior of the $K\gamma$ production amplitude. Similarly, a rigorous description of the K^* resonance comes through associating it with a pole singularity at a complex value of the scattering energy, where the mass and width are related to the pole position, and where the residue of the pole yields couplings to $K\pi$ and $K\gamma$.

The relevant $\gamma K \to K\pi$ scattering process can be studied in first-principles lattice QCD in a two-stage process: In the first stage, the discrete spectrum of states with the quantum numbers of $K\pi$ is extracted from two-point correlation

functions that are computed in the finite spatial volume of the periodic lattice, and these energies are used to constrain the elastic $K\pi \to K\pi$ scattering process in one or more partial waves [6]. In the second stage, three-point correlation functions are computed in which the source operators interpolate $K\pi$ finite-volume states, the sink operators interpolate the kaon, and the electromagnetic current is inserted between the two. From these correlation functions, *finite-volume matrix elements* are extracted, but these must undergo correction by a factor which is sensitive to the volume of the lattice and to the $K\pi$ elastic scattering amplitude [7–9]. While the experimental determinations discussed earlier are for real photons, within the lattice QCD calculation it is natural to consider the transition process also as a function of photon virtuality, Q^2.

The only previous applications of this finite-volume formalism to a similar process are to $\gamma\pi \to \pi\pi$ [10–12], where the contribution of the ρ resonance was determined. An important difference between extraction of $\gamma K \to K\pi$ and $\gamma\pi \to \pi\pi$ in lattice QCD is the presence of *both parities* of $K\pi$ in moving-frame irreducible representations [13]. In this case, even though the *vector* $K\pi$ channel is of interest to us, the *scalar* wave also plays a role—while the transition $\gamma K \to (K\pi)_{\ell=0}$ is forbidden by parity and angular momentum conservation, the *normalization of the finite-volume states* depends upon the elastic $K\pi$ S-wave scattering amplitude. In this paper we will, for the first time, account for this effect in an explicit calculation, showing that application of the finite-volume formalism leads to consistent infinite-volume amplitudes.

In order to sample a wide region of the $E^\star_{K\pi}$ dependence of the transition process, from threshold, through the K^* resonance, and into the high-energy tail, we make use of optimized operators to access correlation functions for $K\pi$ finite-volume states *beyond the ground-state* in each irrep [14]. We use up to the second excited state in some irreps, observing no significant increase in statistical uncertainty relative to the ground states. To sample a large number of points in photon virtuality Q^2 we consider many momenta for the kaon operator, the $K\pi$ operator and the current insertion. We obtain a dataset of 128 unique $(Q^2, E^\star_{K\pi})$ points at 18 values of $E^\star_{K\pi}$ which we describe with parametrizations of the transition amplitude.

In this first calculation we compute the transition $\gamma K \to K\pi$ in the $I = \frac{1}{2}, I_z = +\frac{1}{2}$ isospin state, which is related to the definite charge final states by appropriate isospin Clebsch-Gordan coefficients,

$$\left| K\pi\left(\frac{1}{2}, +\frac{1}{2}\right) \right\rangle = -\frac{1}{\sqrt{3}} |K^+\pi^0\rangle - \sqrt{\frac{2}{3}} |K^0\pi^+\rangle.$$

These factors are such that if one considers the final state K^0 to be a superposition of the decay eigenstates (K^0_S, K^0_L), then we would expect equal decay rates of K^{*+} to $K^+\pi^0$, $K^0_S\pi^+$, and $K^0_L\pi^+$.

TABLE I. Parameters of the lattice configurations used in this calculation. See Ref. [17] for more details.

$(L/a_s)^3 \times (T/a_t)$	$24^3 \times 256$
N_{cfgs}	348
N_{vecs}	160
$a_t m_\pi$	0.04735(22)
$a_t m_K$	0.08659(14)
$\xi = a_s/a_t$	3.455(6)

The parameters of the anisotropic $2 + 1$ flavor Clover lattice used in this calculation are given in Table I, and details of the lattice action can be found in Refs. [15,16]. Using the Ω-baryon mass to set the scale, the pion here has a mass of 284 MeV, and the lattice has a spatial extent of $\sim$2.7 fm. This calculation takes advantage of the prior determination on this lattice of the $K\pi$ spectrum and elastic $K\pi$ scattering amplitudes as reported in Ref. [17]. Herein we use slightly fewer configurations than in that calculation, with the same[1] number of distillation vectors [18], but the extracted discrete energy levels are found to be statistically compatible with those presented therein. The fact that we are using only a single lattice volume means that we are able to use single-elimination jackknife to propagate uncertainty through the entire calculation using the original ensemble of lattice configurations.

II. INFINITE-VOLUME TRANSITION AMPLITUDE

Initial production of a $(K\pi)_{\ell=1}$ system when a photon is absorbed by a kaon is unavoidably followed by strong rescattering of the $K\pi$ system, subject to the constraint of unitarity. Considering the time-reversed $K\pi \to \gamma K$ process, a solution[2] to the unitarity constraint for the transition amplitude takes the form[3]

$$\mathcal{H}^\mu_{\lambda_{K\pi}}(\mathbf{p}_K, \mathbf{p}_{K\pi}; Q^2, E^\star_{K\pi})$$
$$\equiv \langle K; \mathbf{p}_K | j^\mu(0) | K\pi(\ell = 1, \lambda_{K\pi}); E^\star_{K\pi}, \mathbf{p}_{K\pi}\rangle,$$
$$= \mathcal{A}^\mu_{\lambda_{K\pi}}(\mathbf{p}_K, \mathbf{p}_{K\pi}; Q^2, E^\star_{K\pi}) \cdot \frac{1}{k^\star_{K\pi}} \cdot \mathcal{M}^{\ell=1}(E^\star_{K\pi}). \quad (1)$$

The function $\mathcal{A}$ parametrizes the production process and is expected to be a relatively featureless function of $E^\star_{K\pi}$, having neither the unitarity branch cut, nor any possible resonance pole singularities, both of which live in the

---

[1]There is a typographic error in Table I of Ref. [17] which suggests that 162 vectors were used, when in fact the actual number was 160 vectors, as in the current calculation.

[2]This is not a *unique* solution to the unitarity constraint. Another commonly made choice is to make use of the Omnès function, which implements some additional properties of analyticity using a dispersion relation applied to the elastic scattering phase shift [19].

[3]In this paper all variables with a star superscript are evaluated in the center-of-momentum frame.

elastic scattering amplitude, $\mathcal{M}^{\ell=1}$. The factor of $1/k^{\star}_{K\pi}$, featuring the momentum of the kaon (or the pion) in the center-of-momentum frame, is included to cancel the unwanted final-state P-wave threshold factor in $\mathcal{M}$ describing $K\pi \to K\pi$, when we are considering $K\pi \to K\gamma$.

The production amplitude depends upon the helicity of the $K\pi$ state and the direction of the current.[4] The constraints arising from Poincare symmetry can be satisfied by introducing a *kinematic factor* multiplying a *transition form factor*,

$$\mathcal{A}^{\mu}_{\lambda_{K\pi}}(\mathbf{p}_K, \mathbf{p}_{K\pi}; Q^2, E^{\star}_{K\pi})$$
$$= \frac{2}{m_K} \epsilon^{\mu\nu\rho\sigma}(\mathbf{p}_K)_{\nu}(\mathbf{p}_{K\pi})_{\rho}\epsilon_{\sigma}(\mathbf{p}_{K\pi}, \lambda_{K\pi}) \cdot F(Q^2, E^{\star}_{K\pi}). \quad (2)$$

Alternative forms for the kinematic factor are presented in Ref. [11] where they are shown to be equivalent to this one. For physical scattering with spacelike, or modestly timelike photon virtualities, $F(Q^2, E^{\star}_{K\pi})$ should be a real function without nearby singularities.

In the case we are to consider of $K\pi$ in a P wave, we expect there to be a relatively narrow K^* resonance that will manifest as a pole singularity in $\mathcal{M}$ at a complex value of $E^{\star}_{K\pi} = m_R - i\Gamma_R/2$, and this pole will also be present in $\mathcal{H}$. The residue of this pole in $\mathcal{H}$ can be used to provide a rigorous definition of the resonance transition form factor, $K^* \to K\gamma$. The scattering amplitude near the pole can be written as

$$\mathcal{M}(E^{\star}_{K\pi}) = 16\pi \frac{(c_R)^2}{(m_R - i\Gamma_R/2)^2 - E^{\star 2}_{K\pi}} + \cdots,$$

and it follows that the singular part of the transition amplitude, $\mathcal{H}^{\mu}$, takes the form

$$(K^{\mu}F\sqrt{16\pi}\hat{c}_R) \cdot \frac{1}{(m_R - i\Gamma_R/2)^2 - E^{\star 2}_{K\pi}} \cdot (\sqrt{16\pi}\hat{c}_R k^{\star}_{K\pi}),$$

where the reduced couplings $\hat{c}_R \equiv c_R/k^{\star}_{K\pi R}$, and where K^{μ} is the kinematic factor in Eq. (2). The leftmost object is interpreted as the $K^* \to K\gamma$ vertex, and we define a *resonance transition form factor*,

$$f_R(Q^2) \equiv F\left(Q^2, m_R - i\frac{1}{2}\Gamma_R\right) \cdot \sqrt{16\pi}\hat{c}_R, \quad (3)$$

which will be a complex-valued function of the photon virtuality. To obtain this function we must analytically continue $F(Q^2, E^{\star}_{K\pi})$ into the complex energy plane, but since this function does not have the unitarity cut and will

be parametrized by finite-order polynomials in $s = (E^{\star}_{K\pi})^2$, this continuation will be trivial.

Relationships between the quantities introduced in this section, and the partial decay width $\Gamma(K^* \to K\gamma)$ and a cross-section $\sigma(\gamma K \to K\pi)$ will be presented in Sec. VII.

III. TRANSITION PROCESS IN FINITE VOLUME

With an infinite-volume transition amplitude decomposition in hand, we move to consider how the transition process will look in the finite spatial volume of lattice QCD, where the spectrum of $K\pi$ states is not continuous.

The relationship between the discrete spectrum of states in a finite-volume and the infinite-volume scattering amplitudes is now regularly used in lattice QCD (see Ref. [6] and references therein) and takes the form of a quantization condition that can be expressed as

$$0 = \det[F^{-1}(E^{\star}_{K\pi}, \mathbf{p}_{K\pi}; L) + \mathcal{M}(E^{\star}_{K\pi})], \quad (4)$$

where F and $\mathcal{M}$ are matrices which in the current case of elastic $K\pi$ scattering are in the space of possible partial waves $\ell = 0, 1, 2\ldots$. F is a dense matrix of known kinematic functions sensitive to the $L \times L \times L$ volume, while $\mathcal{M}$ is a diagonal matrix of the (*a priori* unknown) elastic scattering amplitudes,

$$\mathcal{M}_{\ell,\ell'} = \delta_{\ell,\ell'} \cdot 16\pi \frac{1}{\rho(E^{\star}_{K\pi})} e^{i\delta_{\ell}(E^{\star}_{K\pi})} \sin\delta_{\ell}(E^{\star}_{K\pi}),$$

where the phase space $\rho = \frac{2k^{\star}_{K\pi}}{E^{\star}_{K\pi}}$. The discrete solutions of Eq. (4) in any given volume, $E^{\star}_n(L)$, are the energy levels expected in a lattice QCD calculation.

The breaking of rotational symmetry by the cubic nature of the lattice boundary means that solutions are sought in irreducible representations, or *irreps*, of the relevant reduced symmetry group. In the case of $K\pi$ scattering, where the scattering hadrons have unequal masses, the subductions of partial waves into these irreps are given in Table II.

The impact of the finite-volume in $1 + j \to 2$ processes can be subsumed into an effective finite-volume normalization for the discrete hadron-hadron states having energies $E^{\star}_n(L)$. When there are multiple partial waves subduced into a particular irrep (or similarly multiple coupled hadron-hadron scattering channels), the finite-volume eigenstates are sensitive to all non-negligible scattering amplitudes. In the case of elastic $K\pi$ scattering in $\mathbf{p}_{K\pi} \neq [000], A_1$ irreps, the state normalizations are sensitive to both S-wave and P-wave scattering amplitudes.[5]

---

[4]Or the helicity of the photon if the amplitude is projected as $\mathcal{H}_{\lambda_{\gamma},\lambda_{K\pi}} = \epsilon^*_{\mu}(\mathbf{q}, \lambda_{\gamma})\mathcal{H}^{\mu}_{\lambda_{K\pi}}$.

[5]The D-wave amplitude is estimated, using energy levels in irreps where $\ell = 2$ is the leading partial wave, to be negligibly small in the energy region we consider [17].

TABLE II. $K\pi$ partial waves of angular momentum $\ell \leq 2$ subduced into irreps in a finite cubic volume—see Refs. [13,20] for more details.

$\mathbf{p}_{K\pi}\Lambda$	$[000]A_1^+$	$[000]T_1^-$	$[100]A_1$	$[100]E_2$	$[110]A_1$	$[110]B_1$	$[110]B_1$	$[111]A_1$	$[111]E_2$	$[200]A_1$	$[100]E_2$
$\ell \leq 2$	0	1	0,1,2	1,2	0,1,2	1,2	1,2	0,1,2	1,2	0,1,2	1,2

Reproducing the basic argument presented in Ref. [21], which itself is a summary and reformulation of the work presented in Refs. [7–9], we start with the relationship between the finite-volume current matrix element, and the infinite-volume transition matrix element defined in the previous section,

$$\left|\,_L\langle K|j^\mu(0)|K\pi\rangle_L\right| = \frac{1}{L^3}\frac{1}{\sqrt{2E_K}}\frac{1}{\sqrt{2E_n}}(\mathcal{H}^\mu \cdot \tilde{R}_n \cdot \mathcal{H}^\mu)^{1/2},$$

(5)

where the residue of the finite-volume $K\pi$ propagator is

$$\tilde{R}_n(\mathbf{p}_{K\pi}, L) \equiv 2E_n \cdot \lim_{E\to E_n}(E-E_n)\left(F^{-1}(E^\star, \mathbf{p}_{K\pi}; L)\right.$$
$$\left. + \mathcal{M}(E^\star)\right)^{-1}.$$

For $K\pi$ scattering at low energies, the finite-volume object F is a dense matrix in a space $(\ell = 0, \ell = 1)$, while $\mathcal{M}$ is a diagonal matrix in that space.[6] Using an eigendecomposition of $F + \mathcal{M}^{-1} = \sum_i \mu_i \mathbf{w}_i \mathbf{w}_i^\mathsf{T}$, we can express $\tilde{R}_n$ in terms of the slope in energy of that eigenvalue which has a zero crossing and hence gives rise to a solution of the quantization condition. The resulting form,

$$\tilde{R}_n = \left(-\frac{2E_n^\star}{\mu_0^{\star\prime}}\right)\mathcal{M}^{-1}\mathbf{w}_0\mathbf{w}_0^\mathsf{T}\mathcal{M}^{-1},$$

factorizes and when used in Eq. (5) reduces the equation to a linear relationship. The presence of an explicit factor of $\mathcal{M}^{-1}$ acts to cancel the rapid energy dependence of $\mathcal{M}$ in Eq. (1). Since the amplitude for $\gamma K \to (K\pi)_{\ell=0}$ is zero by angular momentum and parity, and hence cannot contribute to the finite-volume matrix element, we obtain the result

$$\left|\,_L\langle K|j^\mu(0)|K\pi\rangle_L\right|$$
$$= \frac{1}{L^3}\frac{1}{\sqrt{2E_K}}\frac{1}{\sqrt{2E_n}}\sqrt{-\frac{2E_n^\star}{\mu_0^{\star\prime}}}|\mathbf{w}_0^{\ell=1}|\frac{1}{k_{K\pi}^\star}\mathcal{A}_{\lambda_{K\pi}}^\mu.$$

The finite-volume correction factor in this expression appears repeatedly, so we will give it the symbol

$$\tilde{r}_n^\Lambda(L) = \sqrt{-\frac{2E_n^\star}{\mu_0^{\star\prime}}}|\mathbf{w}_0^{\ell=1}|\frac{1}{k_{K\pi}^\star},$$

(6)

where the dependence on the $K\pi$ irrep, Λ, and the volume, L, is implicit in the finite-volume energy, the eigenvalue slope, and the P-wave component of the eigenvector for each state.

If we define a "finite-volume form factor" via

$$_L\langle K|j^\mu(0)|K\pi; E_n^\star\rangle_L$$
$$= \frac{1}{L^3}\frac{1}{\sqrt{2E_K}}\frac{1}{\sqrt{2E_n}}\cdot K^\mu \cdot F_L(Q^2, E_n^\star),$$

(7)

where K^μ is the same kinematic factor which appears in Eq. (2), then the relationship between finite-volume and infinite-volume form factors is simply

$$F(Q^2, E_{K\pi}^\star = E_n^\star) = \frac{1}{\tilde{r}_n(L)}F_L(Q^2, E_n^\star).$$

(8)

The job of the lattice calculation is to determine finite-volume form factors, F_L, at multiple discrete $(Q^2, E_n^\star)$ points by analyzing the time dependence of appropriate three-point correlation functions. We can then correct for the finite-volume effect using $\tilde{r}$, which can be computed once the $K\pi$ scattering amplitudes in S wave and P wave are known. These scattering amplitudes can be constrained through the quantization condition in Eq. (4) using the discrete energy spectrum obtained in variational analysis of two-point correlation functions.

IV. FINITE-VOLUME SPECTRUM AND $K\pi$ ELASTIC SCATTERING AMPLITUDES

Our approach to determining the lattice QCD spectrum in a range of irreps has been described in detail elsewhere [6,17,22,23], but in short, we make use of a large basis of both "single-meson-like" and "meson-meson-like" operators to compute a matrix of correlations functions, which is then analyzed variationally by solving a generalized eigenvalue problem. The eigenvalues of this problem as a function of time slice are fitted to obtain the discrete energy values, while the eigenvectors provide the weights in a linear superposition of the original operators which optimally overlap with each state in the spectrum. We will later make use of these optimized operators to access three-point correlation functions featuring excited states [14].

---

[6]Except in those irreps listed in Table II which do not feature $\ell = 0$, where these objects are just scalars if we neglect the impact of higher angular momentum partial waves.
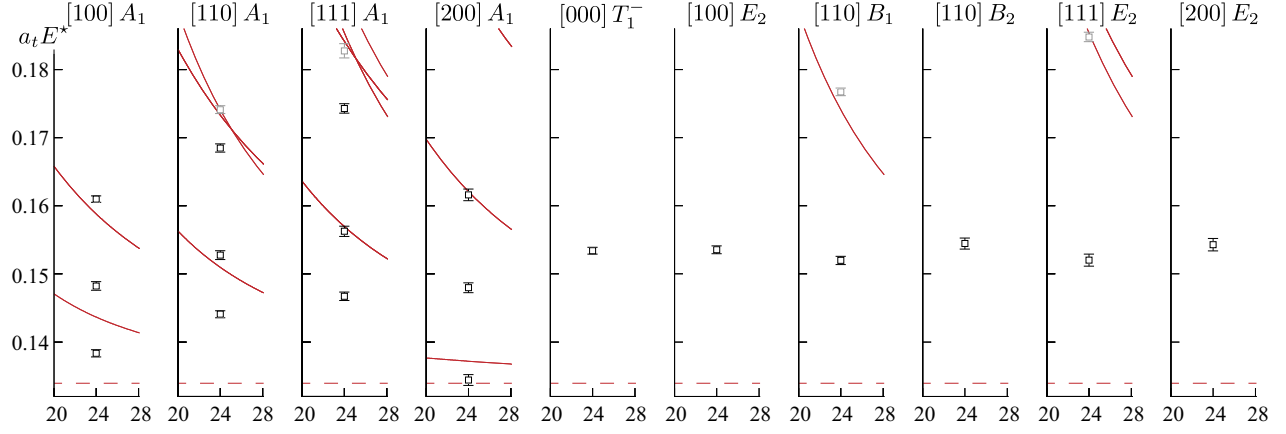
FIG. 1. Finite-volume spectra by irrep extracted from variational analysis of matrices of correlation functions. Solid red curves indicate noninteracting $K\pi$ energy levels and the dashed red line the $K\pi$ threshold. The first inelastic threshold, into $K\pi\pi$, is at $a_t E^\star = 0.181$. Energy levels indicated by gray points are not used in the subsequent transition matrix-element analysis.
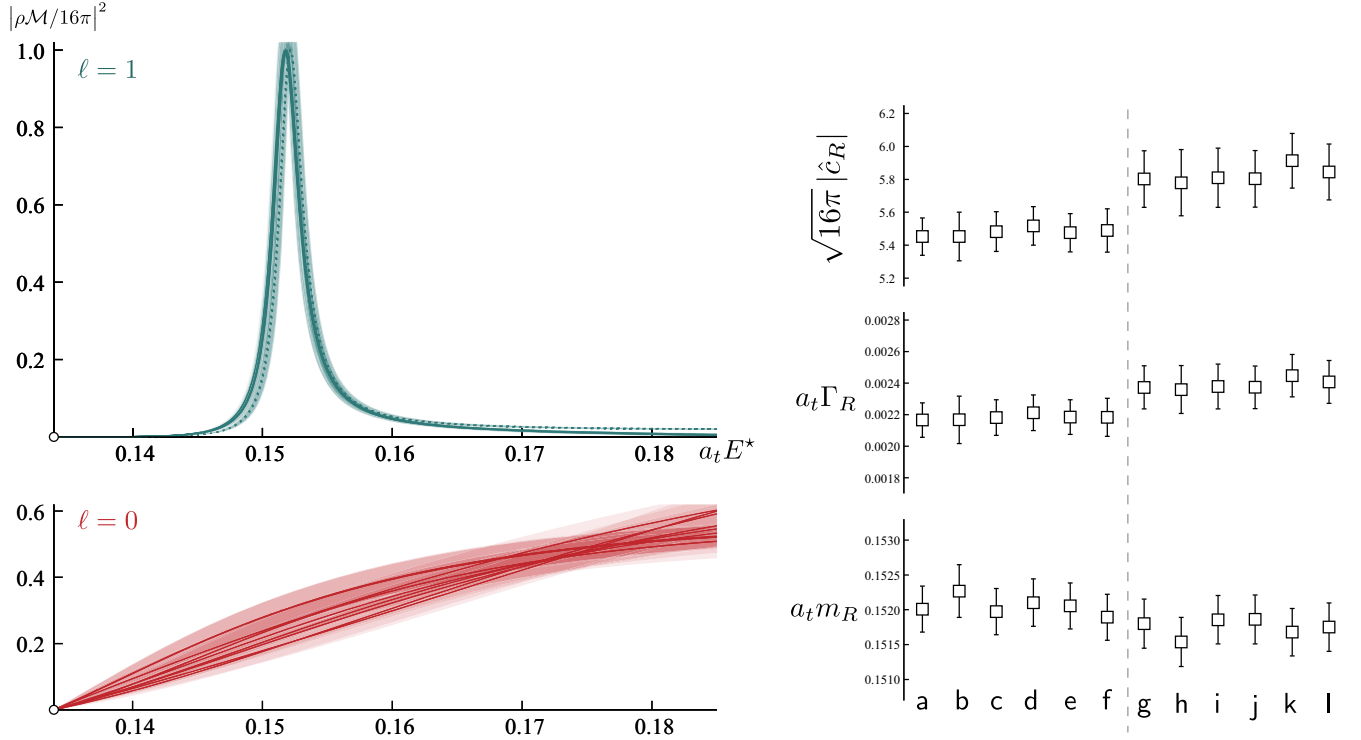

FIG. 2. Left panel: elastic $K\pi$ scattering amplitudes in P and S waves determined using the finite-volume spectra in Fig. 1. Twelve different amplitude parametrizations are used, generating the visible spread in the lower panel, and the more modest spread in the upper panel. In the upper panel, parametrizations using a P-wave Breit-Wigner form are indicated by the dashed lines. Right panel: K^* pole parameters obtained by analytic continuation into the complex plane of the 12 P-wave amplitude parametrizations.

The current system of elastic $K\pi$ scattering[7] was previously considered in Ref. [17] using a slightly larger number of configurations. The spectra extracted in this calculation, shown in Fig. 1, are statistically compatible with the spectra in Ref. [17]. The irreps in the six rightmost columns, which receive no contribution from S-wave scattering, have a clear isolated state near to $a_t E^\star = 0.152$ which signals the presence of a narrow resonance in P wave. Using all these irrep spectra as constraint, plus the $[000]A_1^+$ irrep, solving the quantization condition using parametrizations of S-wave and P-wave elastic scattering leads to the amplitudes shown in Fig. 2.

---

[7]The system is elastic up to $a_t E^\star = 0.181$ where $K\pi\pi$ opens, followed immediately by $K\eta$.

As was previously reported in Ref. [17], there is a well-determined narrow K^* resonance in P wave, while the S wave shows a slow growth from threshold, that may or may not be due to a broad κ resonance. Our focus in this paper is on the K^* resonance, and in order to explore the sensitivity to amplitude parametrization we make use of 12 different choices: six amplitudes having a Breit-Wigner description of the P wave, and various descriptions of the S wave ($BW_{a...f}$), and six amplitudes in which the P wave is described by a K matrix featuring a single pole plus a polynomial ($KM_{g...l}$). More complete descriptions of the amplitudes are given in Appendix C.[8]

We observe in Fig. 2 that the P-wave amplitude is largely insensitive to the details of the parametrization, with the only notable feature being the more rapid fall off at energies well above the resonance for the more flexible K-matrix forms relative to the Breit-Wigner form. Also shown in Fig. 2 are the P-wave resonance pole parameters for the 12 variations, and we note that compared to the K-matrix forms, the Breit-Wigner forms have a resonance mass that is slightly higher, and widths and reduced couplings that are systematically slightly smaller. In subsequent analysis we will default to amplitude KM_g, which has resonance pole parameters,

$$a_t m_R = 0.1518(4),$$
$$a_t \Gamma_R = 0.0024(1),$$
$$\sqrt{16\pi}\hat{c}_R = 5.80(17) - i0.19(3),$$

and consider the others as systematic variations.

V. THREE-POINT CORRELATION FUNCTIONS

In order to access finite-volume transition matrix-elements we compute three-point correlation functions having an optimized kaon operator[9] at a definite momentum $\mathbf{p}_K$ at a fixed timeslice $\Delta t/a_t = 32$, an optimized $K\pi$ operator at a definite momentum $\mathbf{p}_{K\pi}$ in an irrep Λ[10] at a fixed timeslice 0, and an insertion of the spatially directed electromagnetic current, projected to definite momentum $\mathbf{q} = \mathbf{p}_K - \mathbf{p}_{K\pi}$, at each timeslice t/a_t between 0 and 32.

The optimized operators are normalized such that

$$\langle n'|\Omega_n^\dagger(0)|0\rangle = \sqrt{2E_n}\delta_{n,n'} + \dots,$$

and it follows that the three-point correlation functions have a spectral decomposition,

$$\langle 0|\Omega_K(\mathbf{p}_K, \Delta t)j(\mathbf{q}, t)\Omega_{K\pi}^\dagger(\mathbf{p}_{K\pi}, 0)|0\rangle$$
$$= L^3\sqrt{2E_K}\sqrt{2E_n}e^{-E_K(\Delta t - t)}e^{-E_n t} \cdot {}_L\langle K|j(0)|K\pi; E_n^\star\rangle_L$$
$$+ \dots, \qquad (9)$$

where the ellipsis represents possible suppressed contributions from source and sink states other than the ones optimally produced by the source and sink operators. Using our definition of a "finite-volume form-factor" in Eq. (7), we obtain

$$\langle 0|\Omega_K(\mathbf{p}_K, \Delta t)j(\mathbf{q}, t)\Omega_{K\pi}^\dagger(\mathbf{p}_{K\pi}, 0)|0\rangle$$
$$= e^{-E_K(\Delta t - t)}e^{-E_n t} \cdot KF_L(Q^2, E_n^\star) + \dots,$$

and from this we can define an effective (timeslice-dependent) form factor that can be constructed by multiplying the correlation function by the appropriate time dependence and dividing by the kinematic factor,

$$F_L(Q^2, E_n^\star; t)$$
$$\equiv e^{E_K(\Delta t - t)} \cdot e^{E_n t} \cdot \frac{1}{K} \cdot \langle 0|\Omega_K(\Delta t)j(t)\Omega_{K\pi}^\dagger(0)|0\rangle. \quad (10)$$

We will describe below how this object is analyzed, but first we turn to the construction of the relevant three-point functions within a lattice QCD computation.

A. Construction of three-point functions

The three-point functions we wish to compute feature the electromagnetic current, $+\frac{2}{3}\bar{u}\gamma^\mu u - \frac{1}{3}\bar{d}\gamma^\mu d - \frac{1}{3}\bar{s}\gamma^\mu s$, and as such the current insertion will appear on both light-quark and strange-quark propagators. The optimized $K\pi$ operators we use at the source are, in general, linear super-positions of both "single-meson-like" operators and "meson-meson-like" operators, and as such the three-point function Wick contractions contain diagrams from both the top and bottom rows of Fig. 3. All these diagrams are computed without further approximation, with the exception of the rightmost entry in each row which features a completely disconnected current insertion—these are more challenging to compute, and are expected to contribute relatively little, indeed they vanish in the limit of exact $SU(3)$ flavor symmetry. These completely disconnected diagrams are not computed. The particular combinations of diagrams that are needed are discussed in Appendix A.

The diagrams we compute require, in addition to light and strange perambulators describing quark propagation within the distillation framework [18], also "generalized perambulators" which carry the current insertion. The $(0 \to t \to \Delta t)$ versions of these are described in Ref. [14], while the

---

[8]Previous studies of the energy dependence of $K\pi$ $I = \frac{1}{2}$ elastic scattering within lattice QCD [24–27] have used similar parametrizations, being typically some variant of a Breit-Wigner form for the P wave, and something similar to an effective-range expansion in the S wave.

[9]Constructed from the linear superposition of "single-hadron-like" operators that gave the ground state in variational analysis of two-point correlation functions.

[10]Taken from the analysis described in the previous section.
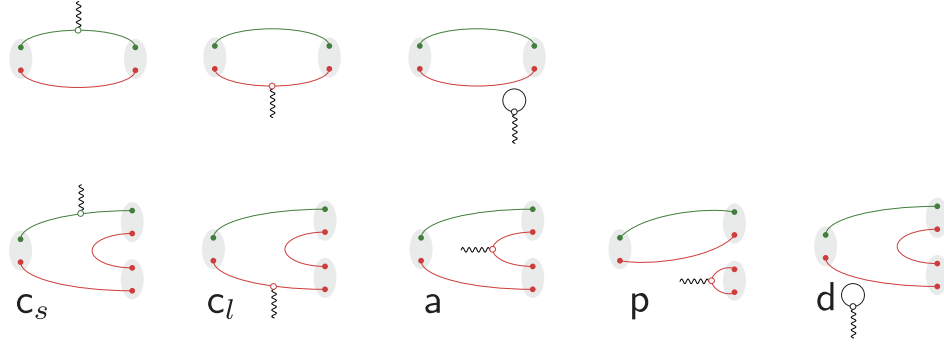
FIG. 3. Wick diagrams required in the computation of three-point functions needed to determine $\gamma K \to K\pi$. In each diagram timeslice 0 is on the right and Δt is on the left. Red lines represent light-quark propagation, and green lines strange-quark propagation. The rightmost diagram in each row includes a completely disconnected loop in which all three quark flavors participate—the electric charges are such that in the limit of equal quark masses these sum to zero. The weights of these diagrams in the construction of the correlation functions we use are presented in Appendix A.

extension for the case $(0 \to t \to 0)$ needed for the third and fourth diagrams in the bottom row is straightforward.

The renormalized electromagnetic current can be expressed as

$$j_{\text{em,phys}} = Z_V^l \left(\frac{1}{\sqrt{2}} j_{\rho,\text{lat}} + \frac{1}{3\sqrt{2}} j_{\omega_l,\text{lat}} \right) + Z_V^s \left(-\frac{1}{3} j_{\omega_s,\text{lat}} \right),$$

$$(11)$$

where isospin-basis currents are

$$j_\rho \equiv \frac{1}{\sqrt{2}} (\bar{u}\Gamma u - \bar{d}\Gamma d), \quad j_{\omega_l} \equiv \frac{1}{\sqrt{2}} (\bar{u}\Gamma u + \bar{d}\Gamma d), \quad j_{\omega_s} \equiv \bar{s}\Gamma s.$$

On the anisotropic Clover-improved lattices used here, the appropriate current includes a tree-level $\mathcal{O}(a)$ improvement term,[11] such that for a spatially directed insertion,

$$\bar{\psi}\Gamma\psi = \bar{\psi}\gamma_i\psi + \frac{1}{4}(1 - \xi)a_t\partial_4(\bar{\psi}\sigma_{4i}\psi).$$

The light- and strange-quark current renormalization factors are determined nonperturbatively using calculations of the charged pion and kaon electromagnetic form factors at zero virtuality, which should both be equal to the electromagnetic charge of these particles, 1. Considering

$$\langle \pi^+(\mathbf{p})|j^i_{\text{em,phys}}|\pi^+(\mathbf{p})\rangle = F^{\pi^+}_{\text{em}}(Q^2 = 0) \cdot 2p^i$$

$$= Z_V^l \frac{1}{\sqrt{2}} \langle \pi^+(\mathbf{p})|j^i_{\rho,\text{lat}}|\pi^+(\mathbf{p})\rangle,$$

and setting $F^{\pi^+}_{\text{em}}(Q^2 = 0) = 1$ yields

$$Z_V^l = \frac{1}{\frac{1}{\sqrt{2}} \langle \pi^+(\mathbf{p})|j^i_{\rho,\text{lat}}|\pi^+(\mathbf{p})\rangle/2p^i}.$$

The matrix element in the denominator is computed for $\mathbf{p} = [100], [110], [111], [200], [210], [211]$ (averaged over rotations), and the results are shown in Fig. 4(a). A correlated constant fit to the six data points gives $Z_V^l = 0.847(10)$.

Considering the charged kaon,

$$\langle K^+(\mathbf{p})|j^i_{\text{em,phys}}|K^+(\mathbf{p})\rangle = F^{K^+}_{\text{em}}(Q^2 = 0) \cdot 2p^i$$

$$= Z_V^l \frac{1}{\sqrt{2}} \langle K^+(\mathbf{p})|j^i_{\rho,\text{lat}}|K^+(\mathbf{p})\rangle$$

$$+ Z_V^l \frac{1}{3\sqrt{2}} \langle K^+(\mathbf{p})|j^i_{\omega_l,\text{lat}}|K^+(\mathbf{p})\rangle$$

$$- Z_V^s \frac{1}{3} \langle K^+(\mathbf{p})|j^i_{\omega_s,\text{lat}}|K^+(\mathbf{p})\rangle,$$

and noting that the first two matrix elements are equal up to (neglected) disconnected current contributions, setting $F^{K^+}_{\text{em}}(Q^2 = 0) = 1$ yields
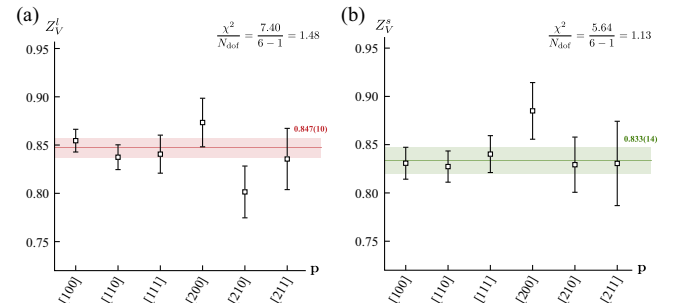

FIG. 4. Vector current renormalization factors for light and strange quarks determined as described in the text.

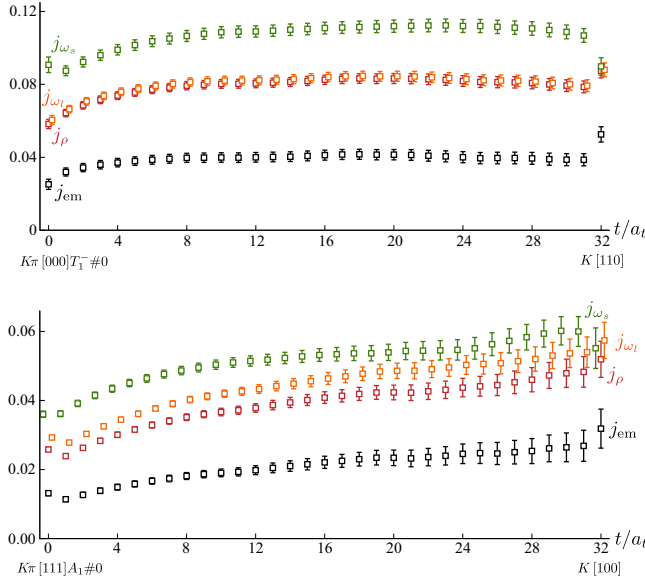
[11] A derivation is presented in Ref. [14].

FIG. 5. Sample three-point functions as in Eq. (9) with the leading time-dependence divided out. Shown are the insertions of the isospin-basis currents, and the relevant combination defined in Eq. (11).

$$Z_V^s = \frac{Z_V^l 2\sqrt{2}\langle K^+(\mathbf{p})|j_{\rho,\text{lat}}^i|K^+(\mathbf{p})\rangle/2p^i - 3}{\langle K^+(\mathbf{p})|j_{\omega_s,\text{lat}}^i|K^+(\mathbf{p})\rangle/2p^i}.$$

Computing the two relevant matrix elements and using the previously obtained value of Z_V^l, we obtain the results shown in Fig. 4(b) and an estimate of $Z_V^s = 0.833(14)$.

Three-point functions of the type given in Eq. (9) using the current in Eq. (11) are constructed by summing weighted combinations of three-point functions computed using the isospin-basis currents. Examples are shown in Fig. 5, where we observe comparable statistical quality for each current.

B. Analysis of three-point functions

We compute a set of three-point functions based upon the following choices:

(i) at $t = 0$, an optimized operator corresponding to each black point in Fig. 1, having any allowed lattice rotation of the specified momentum. If the irrep is more than one dimensional, then all rows are considered;

(ii) at all $0 \le t/a_t \le 32$ a spatial current insertion having momentum [000], [100], [110], [111], or [200] (and *not* rotations of these specific directions). Rather than three Cartesian directions for the current, the subductions of a vector for the relevant momentum are used;

(iii) at $\Delta t/a_t = 32$, an optimized operator for a kaon with a momentum $\le$ [211], with all allowed lattice rotations considered.
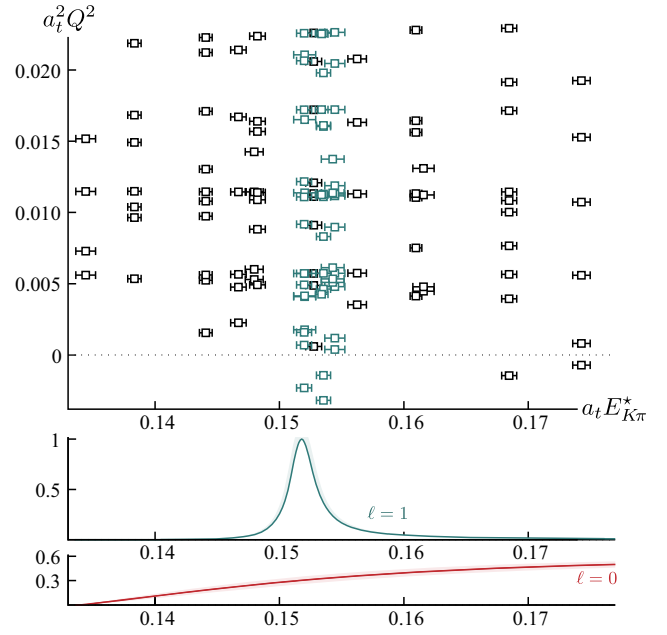

FIG. 6. Kinematic coverage of the $E^\star, Q^2$ plane provided by our computed set of three-point correlation functions. Points in cyan indicate levels in $K\pi$ irreps that have no contribution from $K\pi$ S wave. Also shown for illustration are the KM_g P-wave and S-wave scattering amplitudes over the same $E^\star$ range.

Within these we compute all correlation functions which have a nonzero kinematic factor, K. This leads to over 1000 three-point correlation functions, but many of these correspond to common kinematic points, $(Q^2, E_n^\star)$. In practice we find 128 such points spread over 18 values of $E_n^\star$, distributed as shown in Fig. 6. It is clear that the use of A_1 irreps (which suffer "pollution" from the $K\pi$ S wave) allows access to a much broader region in $E^\star$, along with an increased density of points close to the resonance.

For each computed correlation function, the quantity $F_L(t)$ defined in Eq. (10) is formed, which if the source and sink operators were perfectly optimized would be a constant in time, but which in practice can have curvature from source and/or sink excitation contributions. Correlated fits to the time dependence are carried out using fit forms: a constant, a constant plus a decaying exponential at the source, a constant plus a decaying exponential at the sink, or a constant plus both source and sink exponentials. Such fits are performed for a large number of fit windows in time, and for each such fit, a version of the Akaike information criterion is formed from the χ^2 and the number of degrees of freedom, $w = \exp\left[-\frac{1}{2}(\chi^2 - 2N_{\text{dof}})\right]$. This number is treated as a probability in an average over fits along the lines presented in Ref. [28].[12] In most cases the difference between the value and uncertainty of the extracted constant

---

[12]The average is done on the ensemble of fit values, allowing correlations to be retained.

from the fit window with the highest probability and the value and uncertainty of the "model average" is rather small. The procedure is described in more detail in Appendix D. A small number of correlation functions prove to not have even an approximate plateau region, such that timeslice fits are unreliable—these are excluded from further analysis.

In the large number of cases where there are multiple correlation functions having the same $(Q^2, E_{K\pi}^\star)$ but which differ in momentum directions and/or current insertion irrep, we perform a correlated average of the extracted constant values, to form a single F_L value to be used later. An example of the procedure is presented in Appendix D.

VI. FINITE-VOLUME CORRECTION

As indicated by Eq. (8), the finite-volume form factors, $F_L(Q^2, E_n^\star)$ must be scaled by a factor $1/\tilde{r}_n$ to correctly describe the transition in infinite volume. These factors, $\tilde{r}_n$, computed using Eq. (6), for the amplitude parametrization $\mathrm{KM_g}$, are presented in Fig. 7.

The relative contributions from S-wave and P-wave scattering in finite-volume are quantified by size of

eigenvector components, shown as the red/cyan fractions of each box, recalling that only the P-wave component enters $\tilde{r}_n$ in Eq. (8). In the figure we see clearly that for energy levels in A_1 irreps well below the K^* resonance, there is dominance of the S-wave contribution, with much smaller contributions from the P wave. We observe that the size of $\tilde{r}_n$ can vary considerably between states, but note that the energy levels in non-A_1 irreps lying close to the K^* resonance all have approximately the same value of $\tilde{r}_n$. This is, in fact, the expected behavior when a narrow resonance is present, as we can show that in the limit of a vanishingly small width, for those states lying close to m_R, $\tilde{r}_n \to \sqrt{16\pi}\hat{c}_R$—a derivation is provided in Appendix B.

The degree to which the $\tilde{r}_n$ values are sensitive to the scattering amplitude parametrization is explored in Appendix C, where we observe that the only significant difference is between the Breit-Wigner-based P-wave amplitudes, and the K-matrix-based P-wave amplitudes, and where the largest effect is at energies far from the resonance position, where the Breit-Wigner form may not be accurate.

The upper panel of Fig. 8 shows the complete set of $F_L(Q^2, E_n^\star)$ values extracted from our three-point correlation
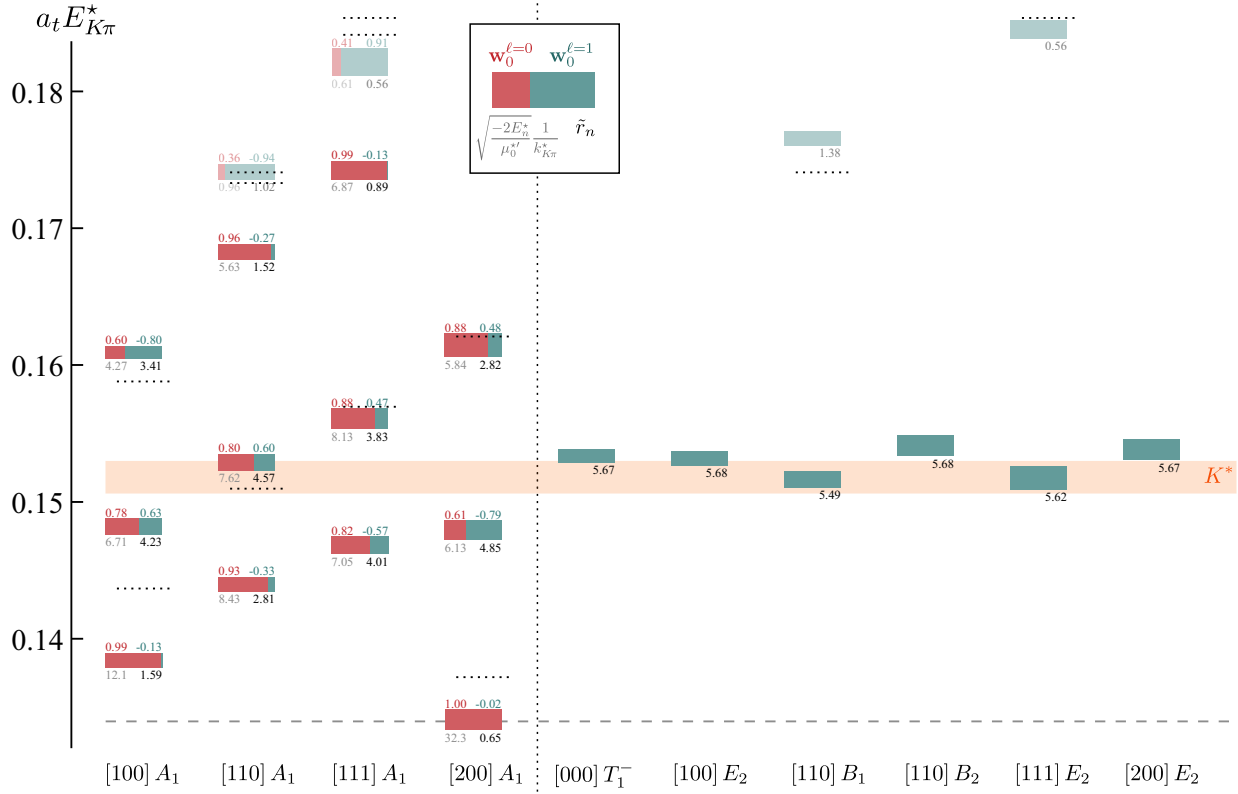

FIG. 7. Components in the construction of the finite-volume normalization factor, $\tilde{r}_n$, defined in Eq. (8) for each discrete energy level using the amplitude $\mathrm{KM_g}$. The red/cyan coloring indicates the relative contribution of $\ell = 0, \ell = 1$ to the eigenvector, normalized as $(\mathbf{w}_0^{\ell=0})^2 + (\mathbf{w}_0^{\ell=1})^2 = 1$. The vertical height of each box indicates the statistical uncertainty on the energy level. Small dashed lines show the $K\pi$ noninteracting energies for this lattice volume, and the location of the K^* resonance ($m_R - \frac{1}{2}\Gamma_R : m_R + \frac{1}{2}\Gamma_R$) is indicated by the orange band.
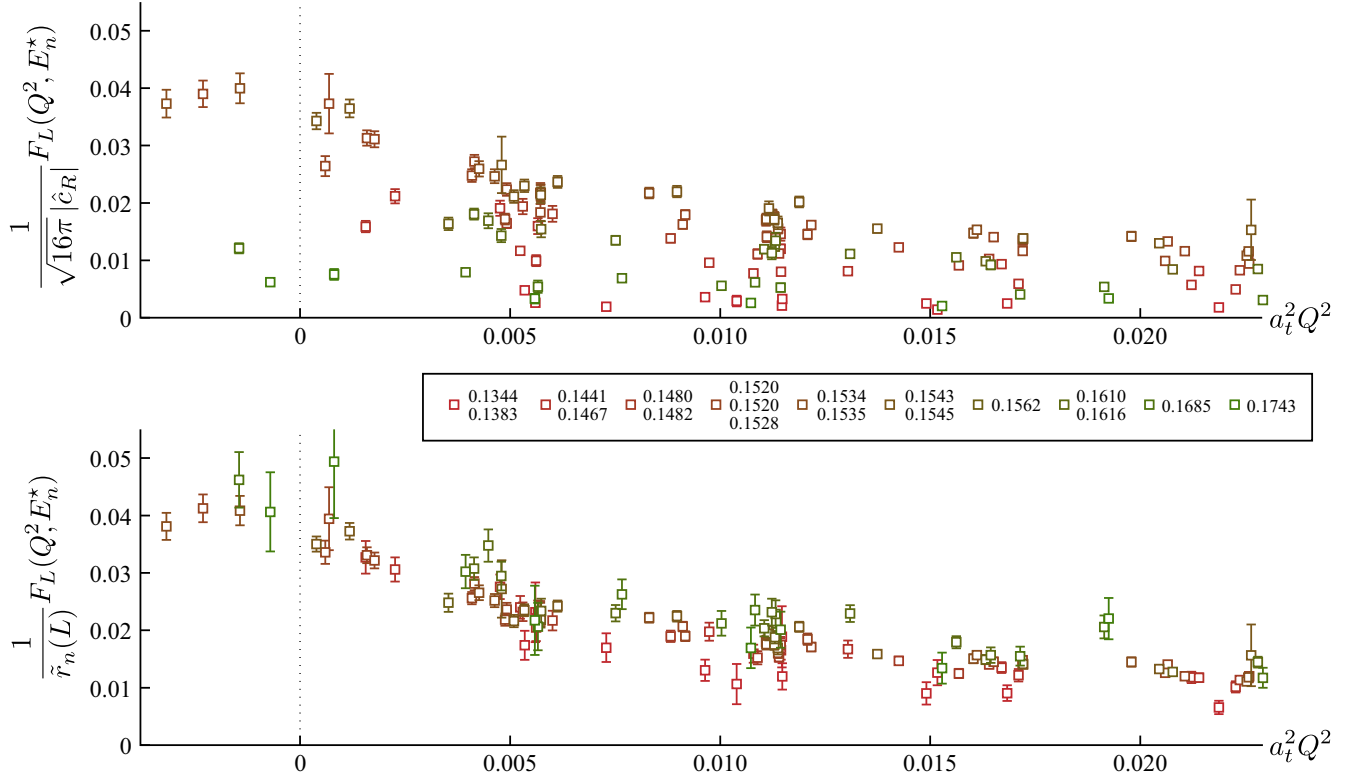
FIG. 8.   Upper panel: finite-volume form-factor values, F_L, extracted from three-point correlation functions, scaled by the constant $K^* \to K\pi$ reduced coupling, as a function of Q^2. Colors indicate $E_n^\star$ ranges. Lower panel: infinite-volume form-factor values, obtained by finite-volume correcting F_L according to Eq. (8). $\tilde{r}_n$ computed using $K\pi$ amplitude parametrization KM$_g$.

functions, scaled by a common constant. It is quite clear that the data show a considerable degree of scatter, and no obvious trend with increasing energy, $E_n^\star$. The lower panel of the figure shows the same data after correction by a factor of $1/\tilde{r}_n$, where the data comes into close agreement, with only a gentle increase in magnitude with increasing $E_n^\star$ remaining.

Another way to illustrate the impact of the finite-volume correction is to examine the data points binned in relatively small Q^2 bins, as shown in Fig. 9. The (uncorrected) black points show significant energy dependence, and scatter far outside the statistical uncertainties,[13] while the (corrected) red points show the much milder energy dependence expected of this infinite-volume quantity.

The corrected data shown in Figs. 8 and 9 supplies the input to the next stage of the calculation, where we seek to parametrize the Q^2 and $E^\star$ dependence of $F(Q^2, E^\star)$ in order to obtain a description of all the data. We take two different approaches to this, motivated by the observation that after finite-volume correction, the resulting 128 data points are found to have a considerable degree of data

correlation whose origin is in the high degree of correlation between the $\tilde{r}_n$ values for different energy levels.

The first approach, which we call "level-by-level fitting," circumvents the high degree of correlation by first fitting the Q^2 dependence of the uncorrected $F_L(Q^2, E_n^\star)$ for each energy level. The parameters in these fits are, where necessary, corrected with $\tilde{r}_n$, and then considered as functions of $E^\star$. The $E^\star$ behavior of the parameters is then fitted, yielding a parametrization of $F(Q^2, E^\star)$.

The second approach, which we call "global fitting," attempts to fit all of the corrected data $F(Q^2, E^\star)$ simultaneously, using an appropriate truncation of the data correlation matrix. We will find that we obtain compatible results from the two methods, utilizing within each a range of parametrization forms to assess systematic variations.

A. Level-by-level fitting

In this approach, for each $K\pi$ energy level, we consider the Q^2 dependence of the uncorrected F_L, for which we typically have a handful of discrete points in Q^2 (as can be seen in each vertical slice of Fig. 6). Figure 10 shows a sample of this kind of fitting for five energy levels.

The selection of parametrizations need not be sophisticated—since no attempt will be made to analytically continue in Q^2, all that is really required are functions

---

[13]Note that the "bumplike" structure in this data is nothing like the line shape of the K^* resonance which is a much sharper peak about $a_t E^\star \approx 0.152$.
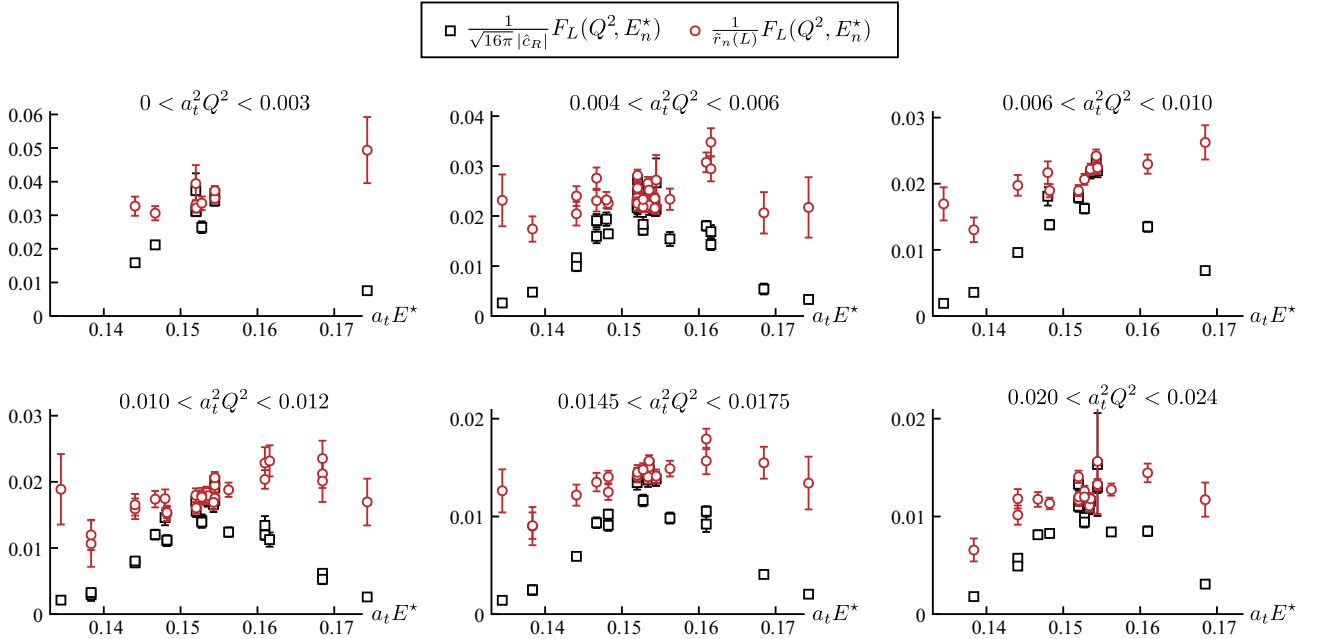
FIG. 9. Finite-volume (black squares) and infinite-volume (red circles) form-factor values in bins of Q^2.

which can interpolate the data points along a limited region of the real Q^2 axis. In practice, we are mostly interested in $Q^2 = 0$ to yield the real-photon transition.[14]

One form which proves capable of describing the data is an exponential of a polynomial in Q^2,

$$F_L(Q^2) = f_{0L} \cdot \exp\left[-\sum_{n=1}^{N} a_n \left(\frac{Q^2}{4m_\pi^2}\right)^n\right]. \quad (12)$$

This is a phenomenological form with no particularly good physics justification, but it is at least free from unphysical nearby singularities. $4m_\pi^2$ is introduced into a ratio with Q^2 as an appropriate dimensionful scale to render the parameters $\{a_n\}$ dimensionless. The subscript L on f_0 indicates that this parameter will require finite-volume correction, while the parameters $\{a_n\}$ do not.

Another option with somewhat more physical motivation (see e.g., Ref. [29]), is a polynomial in a conformal mapping variable $z(Q^2)$,

$$F_L(Q^2) = \sum_{n=0}^{N} b_{nL} \left(z(Q^2) - z(0)\right)^n, \quad (13)$$

where

---

[14]In principle, if a detailed understanding of the Q^2 dependence was sought, the analysis could be done at the level of the separate isospin currents, which have different singularities at timelike Q^2. In this first calculation only the $j_{\rm em}$ combination is analyzed.

$$z(Q^2) = \frac{\sqrt{Q^2 + t_{\rm cut}} - \sqrt{Q_0^2 + t_{\rm cut}}}{\sqrt{Q^2 + t_{\rm cut}} + \sqrt{Q_0^2 + t_{\rm cut}}}, \quad (14)$$

maps the entire complex Q^2 plane away from the unitarity cut ($Q^2 = -\infty \to -t_{\rm cut}$) into a disk of radius 1 in z. In our case where the isovector vector current features, the appropriate choice for $t_{\rm cut}$ is $(2m_\pi)^2$. We may freely choose the scale Q_0^2 so that the Q^2 range of our dataset (within $a_t^2 Q^2 = -0.005 \to 0.030$) lies in a region symmetrically distributed about $z = 0$. The choice $a_t^2 Q_0^2 = 0.0035$ achieves this. Since the parameters $\{b_{nL}\}$ appear linearly in Eq. (13), they will all require finite-volume correction by a factor $1/\tilde{r}$.

We observe in Fig. 10 that the trend of the data can be captured by these fit forms, over either the full Q^2 range, or over a limited $a_t^2 Q^2 < 0.015$ range. The $\chi^2/N_{\rm dof}$ values for these Q^2 fits can be large, and we suggest that this is not a limitation of the fit forms but rather reflects the scatter in the data points that we put down to fluctuations due to the timeslice fitting approach, and possibly discretization effects. In those cases where there are no timelike Q^2 data points and there are no data points at very low spacelike Q^2 values, we observe that there is some model dependency in the extrapolated value of $F_L(Q^2 = 0)$.

These Q^2 fit forms are used to describe each of our 18 energy levels, yielding values of the parameters in Eqs. (12), (13) at 18 values of $E_n^\star$. These are then appropriately finite-volume corrected with $1/\tilde{r}_n$, and we show the example case of fits using $f_{0L} \cdot \exp\left[-a_1 \frac{Q^2}{4m_\pi^2}\right]$ to describe data points with $a_t^2 Q^2 < 0.015$ in Figs. 11 and 12.
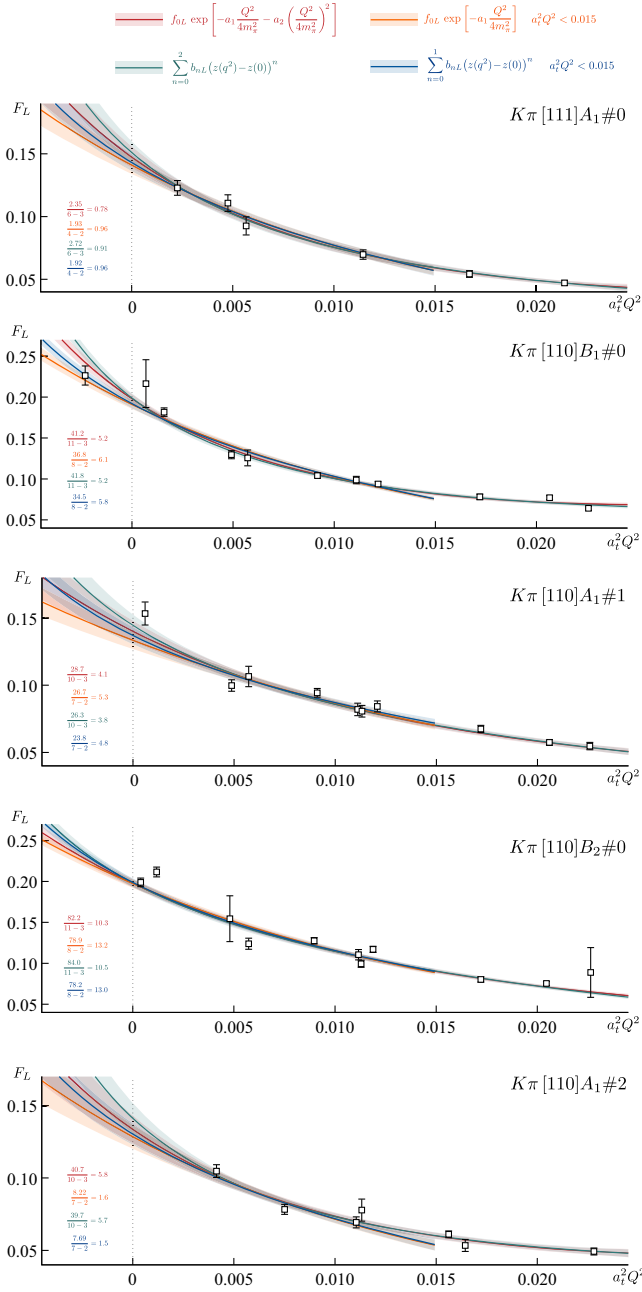
FIG. 10. Fits using Eqs. (12), (13) to the Q^2 dependence of F_L for five sample energy levels. Red, cyan fits to full Q^2 range; orange, blue to limited region, $a_t^2 Q^2 < 0.015$.

The finite-volume corrected $f_0 = f_{0L}/\tilde{r}$ shown in Fig. 11 is observed to have a very mild variation with $E^\star$ over a range that extends well outside the region of the resonance peak. The parameter a_1 which controls the falloff with Q^2, and which does not require finite-volume correction, is seen in Fig. 12 to also have a rather mild dependence on $E^\star$, albeit with some scatter.

Figure 11 illustrates f_0 in the case of finite-volume corrections using the elastic $K\pi \to K\pi$ amplitude parametrization KM_g. The degree of sensitivity to this choice is
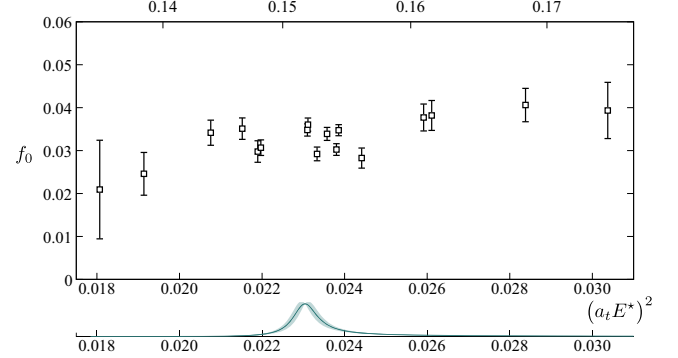
FIG. 11. Energy dependence of $f_0 = f_{0L}/\tilde{r}$ extracted from Q^2 fits using $f_{0L} \cdot \exp\left[-a_1 \frac{Q^2}{4m_\pi^2}\right]$ for $a_t^2 Q^2 < 0.015$, where KM_g amplitude is used for finite-volume correction. Lower panel shows the corresponding KM_g amplitude, indicating the position of the resonance. In this and subsequent plots the upper abscissa shows $a_t E^\star$.
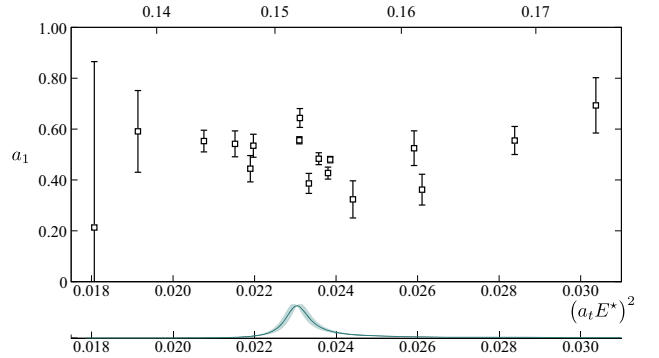
FIG. 12. Energy dependence of a_1 (which requires no finite volume correction) extracted from Q^2 fits using $f_{0L} \cdot \exp\left[-a_1 \frac{Q^2}{4m_\pi^2}\right]$ for $a_t^2 Q^2 < 0.015$.

illustrated in Fig. 13 where it is compared to using BW_a, and where we observe only relatively modest change, most notable at energies away from the resonance, where we expect the Breit-Wigner amplitude to be of lesser validity.

These parameter energy dependences (and similarly those for the other parametrization choices) can be fitted with low-order polynomials in $E^{\star 2}$ to ultimately yield complete parametrizations of $F(Q^2, E^\star)$. We will not show these results here as they prove to be broadly compatible with the results obtained from the more direct "global fitting" approach to be presented in the next subsection.

B. Global fitting

This second approach starts from the complete set of finite-volume-corrected F data points shown in the lower panel of Fig. 8. In principle these 128 data points can be directly fitted with parametrizations that are functions of both Q^2 and $s = E^{\star 2}$. The challenge is that the data
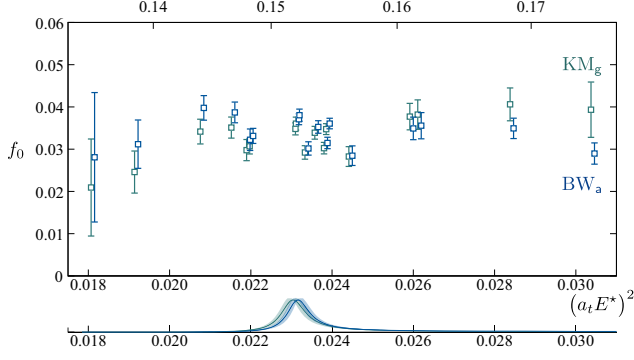
FIG. 13. As Fig. 11, but for two choices of $K\pi \to K\pi$ amplitude parametrization used in the finite-volume correction. BW_a data points displaced slightly to the right for clarity.

correlation matrix for these points features many large positive off-diagonal elements that can be traced back to the high degree of correlation amongst the finite-volume correction factors (which tend to have a fractional uncertainty comparable to the fractional uncertainty on the F_L).

Our calculation makes use of 348 configurations, such that the data correlation matrix is constructed from 348 outer products, and hence has a maximal rank of 348. It is perhaps not such a surprise then that our dimension 128 data correlation matrix has a significant number of small

eigenvalues. The standard procedure of inverting the data correlation matrix for use in the χ^2 leads to fits which lie significantly and systematically below the data points. This motivates us to "reset" smaller eigenvalues, removing the corresponding eigenvectors from the matrix inverse. A discussion of how we select an eigenvalue cutoff of $\lambda_{cut} = 0.01 \cdot \lambda_{max}$ is presented in Appendix E.

The parametrization forms for $F(Q^2, s = E^{\star 2})$ we use are compatible with those used in the approach followed in the previous subsection. For instance,

$$
F(Q^2, s) = \left(f_{0,0} + f_{0,1}\left(\frac{s - s_0}{s_0}\right) + \ldots \right)
$$
$$
\cdot \exp\left[-\left(a_{1,0} + a_{1,1}\left(\frac{s - s_0}{s_0}\right) + \ldots \right)\frac{Q^2}{4m_\pi^2} \right.
$$
$$
\left. -\left(a_{2,0} + a_{2,1}\left(\frac{s - s_0}{s_0}\right) + \ldots \right)\left(\frac{Q^2}{4m_\pi^2}\right)^2 \right.
$$
$$
\left. + \ldots \right], \tag{15}
$$

where a convenient choice is $a_t^2 s_0 = (0.1520)^2$, motivated by the approximate location of the resonance bump in $K\pi \to K\pi$. Alternatively, using the conformal mapping variable,

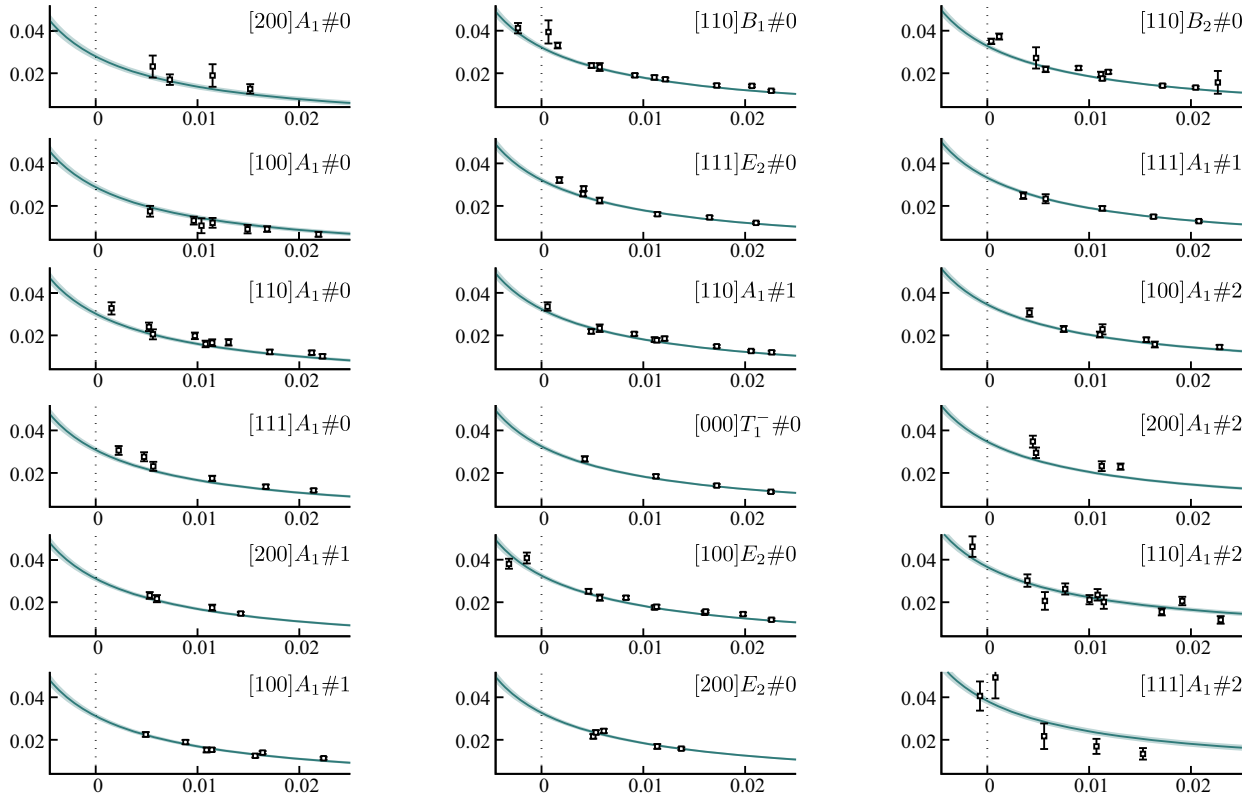FIG. 14. Description of $F(Q^2, E_n^\star)$ data obtained from F_L using amplitude KM_g when fitted with Eq. (17). The curves plotted are "slices" of $F(Q^2, E^\star)$ against $a_t^2 Q^2$ when $E^\star$ is set equal to the finite-volume energies, $E_n^\star$.

$$F(Q^2, s) = \sum_{q=0}^{n_q} \sum_{\sigma=0}^{n_\sigma(q)} b_{q,\sigma} \cdot \left(\frac{s - s_0}{s_0}\right)^\sigma \cdot \left(z(Q^2) - z(0)\right)^q,$$

(16)

so that for example we might have

$$F(Q^2, s) = \left(b_{0,0} + b_{0,1}\frac{s - s_0}{s_0}\right)$$
$$+ b_{1,0} \cdot \left(z(Q^2) - z(0)\right) + b_{2,0} \cdot \left(z(Q^2) - z(0)\right)^2,$$

(17)

which has a universal slope in s for all Q^2.

Figure 14 illustrates the result of a global fit using the form in Eq. (17) when the F_L data is corrected using $\tilde{r}$ computed with amplitude KM$_g$. The fit is able to describe the data with a $\chi^2/N_{\mathrm{dof}} = 81.2/(128 - 91 - 4) = 2.46$, where the subtracted 91 reflects the reduction in information from the resetting of data correlation eigenvalues.

The upper panel of Fig. 15 shows the variation of $F(Q^2 = 0, s)$ under changes in parametrization for fixed choice of $K\pi \to K\pi$ amplitude KM$_g$. Several variations of Eqs. (15) and (16) are considered, all leading to reasonable fits to the data. It is clear that the energy dependence of the

FIG. 15. $F(Q^2 = 0, s)$ from "global fitting." Upper panel shows variation under changes of fit-form using Eqs. (15) and (16). The band bounded by dashed lines shows the choice Eq. (17) as plotted in Fig. 14. Lower panel shows variation under $K\pi \to K\pi$ amplitude choice (felt through the finite-volume corrections, $\tilde{r}_n$) for the fit form Eq. (17).

form factor at zero virtuality is mild, but the precise value of the small slope is not well determined, while the behavior around the resonance is tightly constrained. Figure 15 can be compared to the comparable quantity obtained in the "level-by-level" approach, and plotted in Figs. 11 and 13 where close agreement can be seen.

This "global fitting" procedure was applied to F data corrected with each of the $K\pi \to K\pi$ amplitudes introduced in Sec. IV, BW$_{a\dots f}$, KM$_{g\dots l}$, and the lower panel of Fig. 15 shows the resulting variation in $F(Q^2 = 0, s)$ for a fixed parametrization [Eq. (17)]. There is a clear systematic difference between the P-wave Breit-Wigner amplitudes and those using a K matrix, and the discrepancy is largest away from the resonance region. This effect is observed to be smaller in magnitude than the variation under F parametrization choice shown in the upper panel.

VII. RESULTS

Making use of the transition form factor, $F(Q^2, s)$, obtained in the previous section, we can compute the transition amplitude $\mathcal{H}$, introduced in Eq. (1)—this is shown for three sample photon virtualities in Fig. 16, where we have divided out the kinematic factor to give an invariant quantity. As expected, the K^* resonance bump present in $K\pi$ elastic scattering is also present in the transition amplitude, barely modulated in shape given the mild energy dependence of $F(Q^2, s)$.

As indicated in Eq. (3), the *resonance transition form factor*, $f_R(Q^2)$, can be found by analytically continuing $F(Q^2, s)$ to the location of the resonance pole. We show the result of this in Fig. 17, where the smallness of the imaginary part can be explained by the narrow width of the K^* which causes only a small departure from the real value on the real energy axis.

The value of this quantity at $Q^2 = 0$ is of particular interest, it being the amplitude for a real photon transition. A conservative best estimate from this calculation, accounting for the degree of fluctuation observed when varying the $K\pi$ elastic scattering amplitude, the range of $E^\star$ and Q^2 data considered, and the transition amplitude parametrization, is

$$f_R(0) = 0.185(15) - i0.008(3).$$

(18)

A somewhat comparable[15] quantity can be extracted from the experimental partial decay width, $\Gamma(K^{*+} \to K^+\gamma)$. Given an amplitude for $K^{*+} \to K^+\gamma$,

$$T_{\lambda_{K\pi}, \lambda_\gamma} = e\epsilon_\mu^*(\lambda_\gamma) K^\mu(\lambda_{K\pi}) f,$$

---

[15]Experimental analyses do not typically perform an analytic continuation to the pole, rather they assume a Breit-Wigner energy-dependence and factorize the numerator into production and decay partial widths.
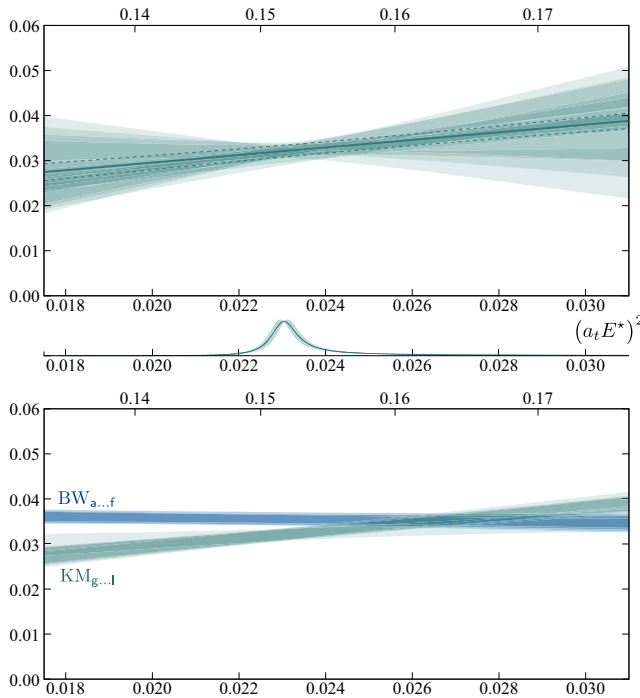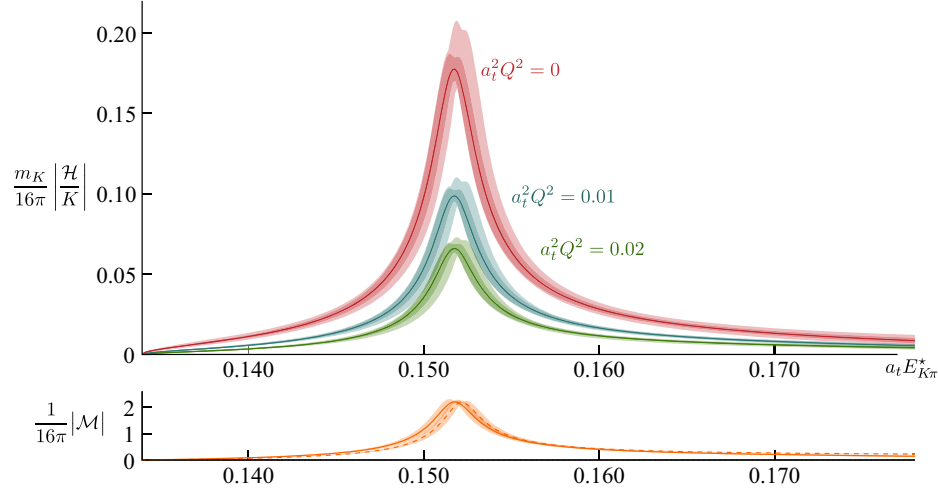
FIG. 16. Transition amplitude for $\gamma K^+ \to (K\pi)_{I=1/2, I_z=+1/2}$ for three values of photon virtuality. Lines and inner band correspond to the "global fitting" analysis using $\mathrm{KM_g}$ for the $K\pi$ elastic scattering amplitude, and Eq. (17) as transition parametrization. The outer band shows an envelope of one-sigma variations over choices of $K\pi$ amplitude and transition amplitude parametrization form. The lower panel shows the corresponding elastic $K\pi$ P-wave scattering amplitude for two sample parametrizations: $\mathrm{KM_g}$ (solid line) and $\mathrm{BW_a}$ (dashed line).

where K^μ is the same kinematic factor defined in Eq. (2), the decay width is given by

$$\Gamma(K^{*+} \to K^+ \gamma) = \frac{4}{3} \alpha \frac{k_{K\gamma}^{\star 3}}{m_K^2} |f|^2.$$

The argument leading up to Eq. (3) suggests an association between $f_R(0)$ and f in the above equations that would be exact for a stable K^*. Using the PDG average [30] for the
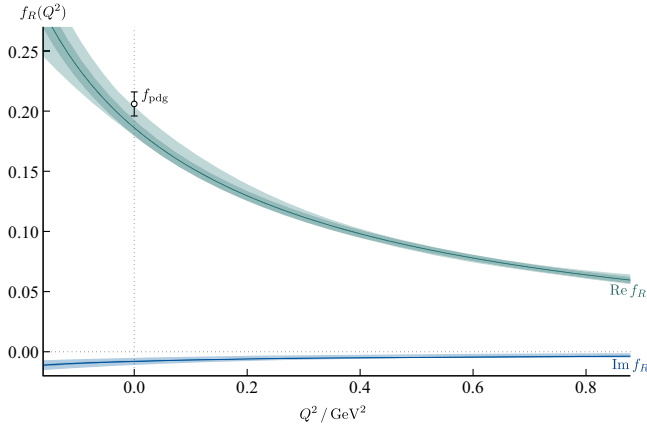
FIG. 17. $K^{*+} \to K^+ \gamma$ resonance transition form factor, as defined in Eq. (3). Lines and inner band correspond to the "global fitting" analysis using $\mathrm{KM_g}$ for the $K\pi$ elastic scattering amplitude, and Eq. (17) as transition parametrization. The outer band shows an envelope of one-sigma variations over choices of $K\pi$ amplitude and transition amplitude parametrization form. Also shown an estimate for the $Q^2 = 0$ value extracted from the experimental radiative decay width.

radiative partial decay width, and the physical values of hadron masses, we extract

$$|f_{\mathrm{pdg}}| = 0.206(10),$$

which we show in Fig. 17. We note that our $|f_R(0)| = 0.185(15)$, despite being computed with unphysically heavy light quark masses, is in reasonable agreement with this value.[16]

The rate of falloff of $f_R(Q^2)$ with Q^2 might be used to estimate a *transition radius* defined, in analogy to the charge radius of stable hadrons, via

$$\langle r^2 \rangle_{K^{*+}, K^+} \equiv \frac{1}{f_R(0)} \cdot \left(-6 \frac{d}{dQ^2} f_R(Q^2) \right)\Bigg|_{Q^2 = 0}.$$

Our calculation suggests (again accounting for systematic variations),

$$\mathrm{Re}\langle r^2 \rangle_{K^{*+}, K^+}^{1/2} = 0.69(4) \text{ fm},$$

and an imaginary part that is much smaller and statistically compatible with zero. This value does not differ significantly from the radius we extract from the charged kaon form factor computed on this same lattice, $\langle r^2 \rangle_{K^+}^{1/2} = 0.55(2)$ fm.

---

[16]The analysis done for $\gamma \pi \to \pi \pi$ in Ref. [31], extended simplistically to the current case, would seem to suggest that it is the quantity f_R / m_K that is approximately constant with changing light quark mass. The kaon mass in this calculation is only 5% larger than the physical kaon mass, leading to a modest correction that worsens slightly the apparent agreement.
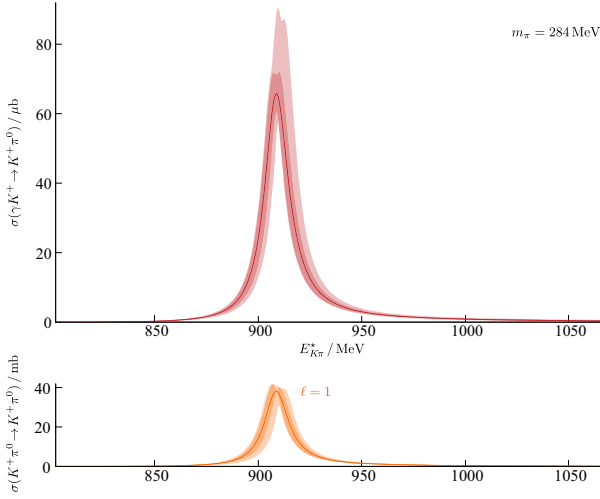
FIG. 18. *P*-wave contributions to cross sections for $\gamma K^+ \to K^+ \pi^0$ and $K^+ \pi^0 \to K^+ \pi^0$ in a version of QCD with $m_\pi = 284$ MeV.

We can use our transition amplitude to compute a cross section for $\gamma K \to K\pi$. The transition amplitude *for a particular final charge state* requires an isospin Clebsch-Gordan coefficient relative to the definite isospin case we have computed, e.g.,

$$\left| \mathcal{H}(\gamma K^+ \to K^+ \pi^0) \right| = \frac{1}{\sqrt{3}} \left| \mathcal{H}(\gamma K^+ \to (K\pi)_{1/2,+1/2}) \right|.$$

We will assume no contribution to this final charge-state from the nonresonant $I = \frac{3}{2}$ channel (which we have not computed).

The differential cross section is related to the transition matrix element in the usual way,

$$\frac{d\sigma}{d\Omega}(\gamma K^+ \to K^+ \pi^0) = \frac{1}{64\pi^2} \frac{k^\star_{K\pi}}{k^\star_{K\gamma}} \frac{1}{s} \cdot \frac{1}{2} \sum_{\lambda_{K\pi}, \lambda_\gamma} \left| \frac{1}{\sqrt{3}} e\epsilon_\mu(\lambda_\gamma) \mathcal{H}^\mu_{\lambda_{K\pi}} \right|^2,$$

where there is an average over the two polarizations of a real photon in the initial state, and a sum over the three helicities of the *P*-wave $K\pi$ final state. The sums can be evaluated, and the integral over solid angle carried out to yield for the cross section,

$$\sigma(\gamma K^+ \to K^+ \pi^0) = \frac{1}{3} \alpha \frac{k^\star_{K\gamma}}{k^\star_{K\pi}} \frac{1}{m^2_K} |F\mathcal{M}|^2,$$

which we plot for this lattice calculation[17] in Fig. 18.

The experimentally measurable Primakoff process in which a kaon beam is scattered off a nucleus, $KA \to K\pi A$, with photon exchange isolated at small Mandelstam t, is

---

[17]Physical units are obtained by setting the lattice scale using the mass of the Ω baryon.

proportional to the version of this cross section for physical mass light quarks, but the data from the 1970s and 1980s was not presented in this way. A recent theoretical study, Ref. [5], built a dispersive representation of the $\gamma K \to K\pi$ process, using as input descriptions of experimental $K\pi$ scattering, and phenomenology to constrain cross channels, with subtraction constants left to be set by other experimental input. When the PDG values of the $K^* \to K\gamma$ radiative widths and the chiral anomaly were used, the resulting cross section had a peak value of around 35 μb, around a factor of 2 smaller than we have found with $m_\pi = 284$ MeV. In Appendix F, we explore (in a simplistic extrapolation model) whether evolution to the physical point is likely to bring the cross section into closer agreement with Ref. [5].

VIII. SUMMARY

We have presented the first lattice QCD determination of the process $\gamma K \to K\pi$, where the vector K^* appears as a resonance. This required careful application of the formalism relating current matrix elements in finite volume to those in infinite volume. In moving-frame A_1 irreps, which provide the broadest coverage of $E_{K\pi}$, the finite-volume correction factor is sensitive to the S-wave scattering amplitude as well as the P-wave scattering amplitude, and our results indicate that this correction does indeed bring the matrix elements extracted from these irreps into good agreement with matrix elements at similar $E_{K\pi}$ extracted from irreps whose correction factor is not sensitive to the S-wave amplitude.

The result of this calculation is the $\gamma K \to K\pi$ amplitude as a function of Q^2 and $E_{K\pi}$ constrained by lattice QCD determined matrix elements at 128 discrete points in the $(Q^2, E_{K\pi})$ plane. The amplitude is constructed to conform to the restriction imposed by elastic unitarity, and the contribution of the K^* resonance is quantified in a rigorous way by analytically continuing to the resonance pole.

The use of a light-quark mass that is somewhat larger than the physical value, yielding a pion mass of 284 MeV, limits our ability to directly compare to related experimental measurements. In advance of a recomputation at the physical light quark mass, one might consider attempting a *chiral extrapolation*, but this is not simple. As emphasized in Ref. [31], in a process like this one, where there is a low-lying resonance, and where unitarity is an important constraint, naive applications of chiral effective field theory are unlikely to be successful. Reference [31] considered the closely related $\gamma\pi \to \pi\pi$ process, using an approach combining dispersion relations with $SU(2)$ chiral perturbation theory, which they applied to extrapolate the lattice QCD data presented in [11,12]. While the extrapolation is likely to be milder in the current case, the poorer convergence of $SU(3)$ chiral perturbation theory may limit the precision that can be obtained.

An obvious future application of the formalism explored in this paper would be to the process $B \to K^* \ell^+ \ell^-$, where experimental measurements are being used to place limits on lepton universality and more generally to limit possible extensions to the Standard Model. Doing this requires precise knowledge of the QCD form factors in the transition $B \to K^*$ induced by the short-distance current of electroweak origin. To date, these have been evaluated in lattice QCD treating the K^* as a stable particle (see for example Ref. [32]) which leaves an undetermined systematic error associated with the resonant nature of the K^*.

APPENDIX A: WICK DIAGRAMS IN $\gamma K \to K\pi$

The correlation functions we require in this calculation include cases in which the source operator is a $K\pi$-like product, and in these cases the Wick diagrams shown in the lower row of Fig. 3 feature. When the $K\pi$-like operator has $(I, I_z) = (\frac{1}{2}, +\frac{1}{2})$, the three isospin-basis current insertions correspond to the following linear combinations of Wick diagrams (up to an overall factor):

$$\langle j_\rho \rangle = -\frac{3}{2}\mathsf{c}_l + \frac{1}{2}\mathsf{a} + \mathsf{p},$$

$$\langle j_{\omega_l} \rangle = -\frac{3}{2}\mathsf{c}_l - \frac{3}{2}\mathsf{a} + 3\mathsf{d}_l,$$

$$\langle j_{\omega_s} \rangle = -\frac{3}{\sqrt{2}}\mathsf{c}_s + \frac{3}{\sqrt{2}}\mathsf{d}_s.$$

In the particular combination of these needed for j_{em}, the diagram a actually cancels, and the disconnected pieces enter proportional to $Z_V^l \mathsf{d}_l - Z_V^s \mathsf{d}_s$ such that in the $SU(3)$ flavor limit, the net disconnected contribution is zero.

We might anticipate that the contribution of diagram p will be small: one way to view it is that the current j_ρ behaves like an isovector, vector meson which transitions to a pion through t-channel exchange of color-singlet isoscalar $C = -$ objects, and diagram p corresponds to the *disconnected* contribution to these. Considered in the t channel, the relevant objects coupling to $\rho^0 \pi^0$ are the h_J and ω_J mesons, and these are not believed to have large disconnected contributions [41]. Diagram p is nevertheless computed without further approximation in our calculation.

For comparison, when the $K\pi$-like operator has $(I, I_z) = (\frac{3}{2}, +\frac{1}{2})$, the three isospin-basis current insertions correspond to the following linear combinations of Wick diagrams (up to an overall factor):

$$\langle j_\rho \rangle = -\sqrt{2}\mathsf{a} + \sqrt{2}\mathsf{p}, \qquad \langle j_{\omega_l} \rangle = 0, \qquad \langle j_{\omega_s} \rangle = 0.$$

APPENDIX B: FINITE-VOLUME NORMALIZATION FOR A NARROW RESONANCE

When a partial wave contains a narrow resonance, the finite-volume normalization factors for discrete energy eigenstates close to the resonance mass take a particularly simple and illustrative form. For simplicity, consider a

single elastic partial-wave of angular momentum ℓ, with a single resonance pole lying close to the real energy axis,

$$\mathcal{M}(E^\star) = 16\pi \frac{(c_R)^2}{(m_R - i\frac{1}{2}\Gamma_R)^2 - E^{\star 2}} + \text{reg}, \quad \text{(B1)}$$

where the pole dominates over the part regular in $E^{\star 2}$ for energies $E^\star \approx m_R$.

For an amplitude like this with Γ_R small, solution of the quantization condition, $0 = \det[F^{-1} + \mathcal{M}]$, in any irrep containing ℓ, for any volume, will yield a discrete energy eigenvalue $E_R^\star(L)$ parametrically close to m_R. The corresponding finite-volume state normalization can be found starting from

$$\tilde{R}_n = 2E_n \cdot \lim_{E \to E_n} (E - E_n) \frac{1}{F^{-1} + \mathcal{M}},$$

by noting that there is no reason for the slope of the finite-volume function F^{-1} to be large at the resonance mass, while the slope of $\mathcal{M}$ is large there so that

$$\left.\frac{dF^{-1}}{dE}\right|_{E=E_R} \ll \left.\frac{d\mathcal{M}}{dE}\right|_{E=E_R},$$

and hence, for the energy-level near the resonance mass,

$$\tilde{R}_R \to \frac{2E_R}{\frac{d\mathcal{M}}{dE}|_{E_R}} = \frac{2E_R^\star}{\frac{d\mathcal{M}}{dE^\star}|_{E_R^\star}}.$$

The factor suggested in Ref. [21], and applied as finite-volume correction in this paper, $\sqrt{-\frac{2E_R^\star}{\mu_0^{\star\prime}}\frac{1}{k^{\star\ell}}}$, in the elastic, single partial-wave case considered here is just $\sqrt{\tilde{R}_n} \cdot \mathcal{M} \cdot \frac{1}{k^{\star\ell}}$. Insertion of Eq. (B1) yields

$$\sqrt{-\frac{2E_R^\star}{\mu_0^{\star\prime}}\frac{1}{k^{\star\ell}}} = \sqrt{16\pi}\frac{c_R}{k^{\star\ell}} + \dots,$$

where the corrections vanish as $\Gamma_R \to 0$. Because the ℓ wave has a threshold behavior $\mathcal{M} \sim (k^\star)^{2\ell}$, it is convenient to define reduced couplings $\hat{c}_R = c_R/k_R^{\star\ell}$, so that for a narrow resonance

$$\sqrt{-\frac{2E_R^\star}{\mu_0^{\star\prime}}\frac{1}{k^{\star\ell}}} = \sqrt{16\pi}\hat{c}_R. \quad \text{(B2)}$$

This volume-independent result is in accord with our decomposition of the infinite-volume transition amplitude, $\mathcal{H} = KF\frac{1}{k^{\star\ell}}\mathcal{M}$, since for the narrow resonance,

$$\mathcal{H} = (KF\sqrt{16\pi}\hat{c}_R) \cdot \frac{1}{(m_R - i\frac{1}{2}\Gamma_R)^2 - E^{\star 2}} \cdot \left(\sqrt{16\pi}\hat{c}_R k^{\star\ell}\right),$$

where the three factors can be interpreted as the $\gamma K \to K^*$ vertex, the K^* propagator, and the $K^* \to K\pi$ vertex. As shown in Eq. (8),

$$F_L = \sqrt{-\frac{2E_R^\star}{\mu_0^{\star\prime}}\frac{1}{k^{\star\ell}}} \cdot F,$$

so for a resonance with a vanishing width,

$$F_L = F\sqrt{16\pi}\hat{c}_R,$$

and the finite-volume computed quantity is indeed the volume-independent (stable) $K^* \to K\gamma$ form factor.

APPENDIX C: $K\pi$ AMPLITUDE PARAMETRIZATIONS

The $K\pi$ elastic scattering amplitude parametrizations we use are a subset of those investigated in Ref. [17], and more details can be found in that paper and in references therein.

For the choices $BW_{a\dots f}$ the P-wave amplitude is a Breit-Wigner form,

$$\mathcal{M}^{\ell=1}(s) = \frac{16\pi}{\rho(s)}\frac{\sqrt{s}\Gamma(s)}{m_{BW}^2 - s - i\sqrt{s}\Gamma(s)}, \quad \Gamma(s) = g_{BW}^2\frac{k^{\star 3}}{s},$$

where m_{BW}, g_{BW} are free parameters. The S-wave amplitudes are

$$\mathcal{M}_a^{\ell=0}(s) = \frac{16\pi}{(\gamma_0 + \gamma_1(\frac{s-s_{thr}}{s_{thr}}))^{-1} + I_{thr}(s)},$$

$$\mathcal{M}_b^{\ell=0}(s) = \frac{16\pi}{(\gamma_0 + \gamma_1(\frac{s-s_{thr}}{s_{thr}}) + \gamma_2(\frac{s-s_{thr}}{s_{thr}})^2)^{-1} + I_{thr}(s)},$$

$$\mathcal{M}_c^{\ell=0}(s) = \frac{16\pi(s - s_A)}{(\gamma_0 + \gamma_1(\frac{s-s_{thr}}{s_{thr}}))^{-1} - i\rho(s)(s - s_A)},$$

$$\mathcal{M}_d^{\ell=0}(s) = \frac{16\pi}{(\gamma_0 + \gamma_1(\frac{s-s_{thr}}{s_{thr}}))^{-1} - i\rho(s)},$$

$$\mathcal{M}_e^{\ell=0}(s) = \frac{16\pi(s - s_A)}{\gamma_0 + \gamma_1(\frac{s-s_{thr}}{s_{thr}}) + I_{thr}(s)(s - s_A)},$$

$$\mathcal{M}_f^{\ell=0}(s) = \frac{16\pi}{\rho(s)}\frac{k^\star}{a^{-1} + \frac{1}{2}rk^{\star 2} - ik^\star},$$

where $I_{thr}(s)$ is the Chew-Mandelstam phase-space subtracted at threshold, $s = s_{thr}$. Amplitudes c and e include Adler zeros with s_A fixed at the tree-level location.
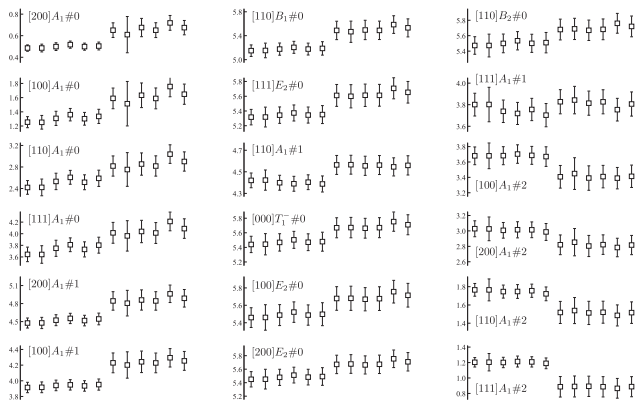
FIG. 19. $\tilde{r}_n$ values by energy level for 12 $K\pi \to K\pi$ scattering amplitude parametrizations a…l as described in the text.

For the choices $KM_{g\ldots j}$, the S-wave amplitude is the same as in amplitude a, while for KM_k the S wave is the same as d, and for KM_l it is the same as e. The P-wave amplitudes are

$$\mathcal{M}_g^{\ell=1}(s) = \frac{16\pi}{\frac{1}{4k^{\star 2}}\left(\frac{g^2}{m^2-s}+\gamma_0\right)^{-1}+I_{\text{pole}}(s)},$$

$$\mathcal{M}_h^{\ell=1}(s) = \frac{16\pi}{\frac{1}{4k^{\star 2}}\left(\frac{g^2}{m^2-s}+\gamma_0+\gamma_1\left(\frac{s-s_{\text{thr}}}{s_{\text{thr}}}\right)\right)^{-1}+I_{\text{pole}}(s)},$$

$$\mathcal{M}_i^{\ell=1}(s) = \frac{16\pi}{\frac{1}{4k^{\star 2}}\left(\frac{\left(g_0+g_1\frac{s-s_{\text{thr}}}{s_{\text{thr}}}\right)^2}{m^2-s}\right)^{-1}+I_{\text{pole}}(s)},$$

$$\mathcal{M}_j^{\ell=1}(s) = \frac{16\pi}{\frac{1}{4k^{\star 2}}\left(\frac{\left(g_0+g_1\frac{s-s_{\text{thr}}}{s_{\text{thr}}}\right)^2}{m^2-s}+\gamma_0\right)^{-1}+I_{\text{pole}}(s)},$$

$$\mathcal{M}_k^{\ell=1}(s) = \frac{16\pi}{\frac{1}{4k^{\star 2}}\left(\frac{g^2}{m^2-s}+\gamma_0\right)^{-1}-i\rho(s)},$$

$$\mathcal{M}_l^{\ell=1}(s) = \frac{16\pi}{\frac{1}{4k^{\star 2}}\left(\frac{g^2}{m^2-s}+\gamma_0\right)^{-1}+I_{\text{pole}}(s)},$$

where $I_{\text{pole}}(s)$ is the Chew-Mandelstam phase space subtracted at the location of the K-matrix pole, $s = m^2$.

Each parametrization pair is used to describe the finite-volume spectrum, which sets the values of the free parameters. From the amplitudes we can compute the finite-volume factors $\tilde{r}_n$ for each state in the spectrum, and these are shown in Fig. 19. The main variation is observed to be between those amplitudes which use a Breit-Wigner form to describe the P wave and those which use a K matrix. We note also the apparently statistically precise factors for the Breit-Wigner choices well above and well below the resonance—this is an artifact of the lack of freedom within the Breit-Wigner amplitude to vary away

from the resonance, a freedom that *is* present in the K-matrix cases.

APPENDIX D: TIMESLICE FITTING APPROACH

We perform correlated fits to the time dependence of each $F_L(t)$ using four fit functions,

$$\begin{aligned} &F_L, \\ &F_L + a_{\text{src}}e^{-\delta E_{\text{src}}t}, \\ &F_L + a_{\text{snk}}e^{-\delta E_{\text{snk}}(\Delta t-t)}, \\ &F_L + a_{\text{src}}e^{-\delta E_{\text{src}}t} + a_{\text{snk}}e^{-\delta E_{\text{snk}}(\Delta t-t)}, \end{aligned}$$

for large numbers of fit windows $[t_{\min}, t_{\max}]$, always with $t_{\max} - t_{\min} \geq 9$. For the second, third, and fourth fit forms, a broad Bayesian prior is placed on the energy-shift parameter(s), $a_t\delta E = 0.15 \pm 0.15$. For each fit, a weight $w = \exp[-\frac{1}{2}(\chi^2 - 2N_{\text{dof}})]$ is computed, and the 30 fits with largest weights are retained. The weights are normalized to sum to one, and the resulting quantities are assigned the meaning of "model probabilities" [28]. The ensemble values of the determined constants $F_{L,i}$ are then averaged using these probabilities, to yield a "model average" estimate of F_L,

$$F_L^{\text{mod avg}} = \frac{\sum_{i=1}^{30} w_i F_{L,i}}{\sum_{i=1}^{30} w_i}.$$

Examples of fits to three sample $F_L(t)$ are shown in Fig. 20, where the left panel in each case shows the single fit with the largest value of w, whose F_L value is indicated by the red band in the right panel. The right panel shows the $F_{L,i}$ value for the 30 largest w fits, and the cyan band shows the "model average." We observe that in these cases the difference between the model average and the single best fit value is not large but that the model average reflects the fact that some fits of comparable w value to the best fit, do differ systematically from the best fit.

In many cases there are multiple $F_L(t)$ at the same kinematic point $(Q^2, E_n^\star)$, and we choose to combine these by fitting each one independently, as described above, and then averaging the results with a correlated fit to a constant. The reason for this can be seen in Fig. 21, where we observe that the different $F_L(t)$, whilst likely plateauing to the same value, have very different excited state pollutions, and quite different signal/noise ratios. The right panel of Fig. 21 shows the result of the averaging of the fitted F_L to yield a single estimate that is used in subsequent computations.
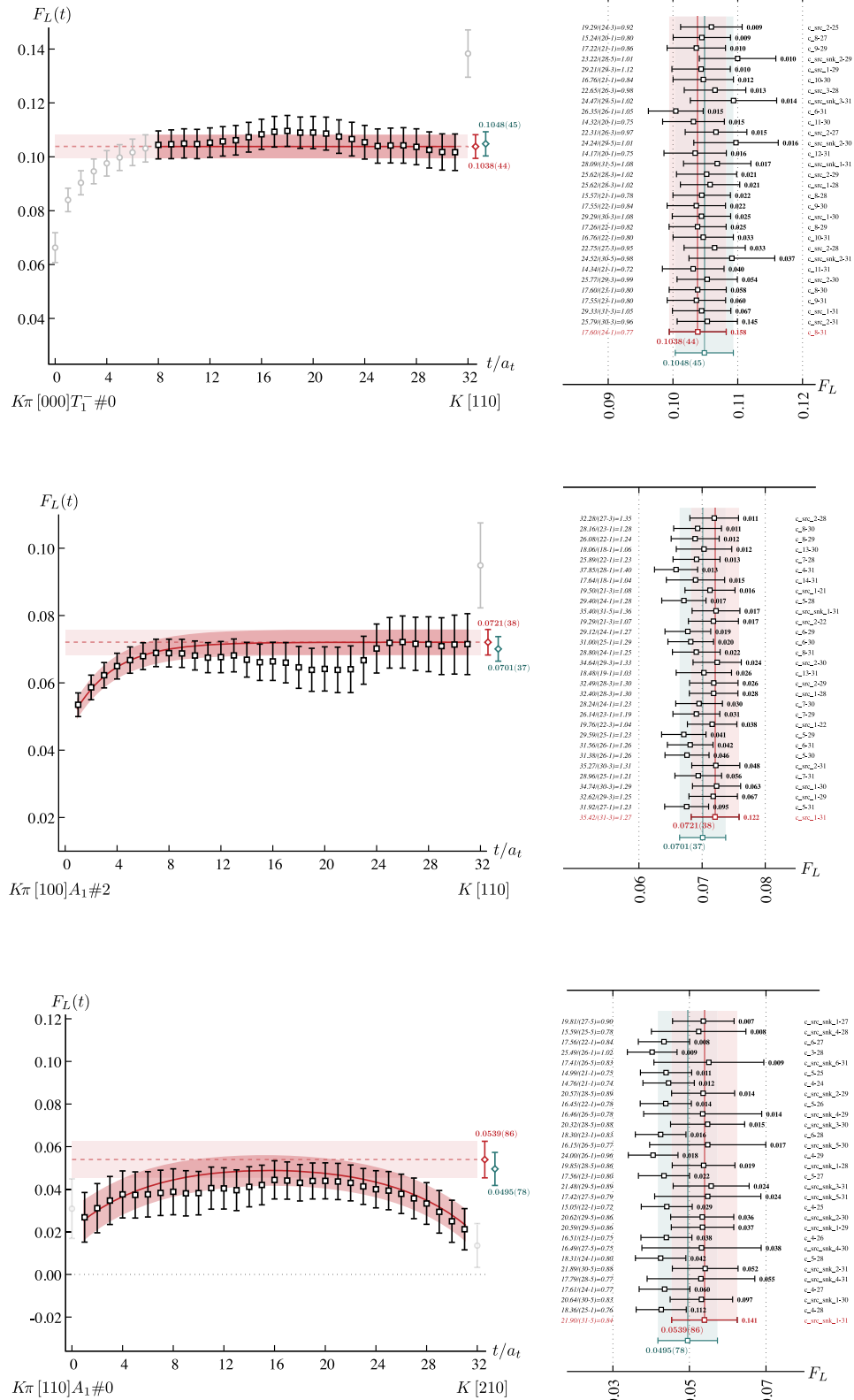
FIG. 20. Fits to timeslice dependence of three sample $F_L(t)$. Left side of each plot shows best single description over varying fit-windows, as quantified by the w_i value. Right side of each plot shows variation over different fit windows with, for each fit, the χ^2/N_{dof} (italic), the fit probability, $\frac{w_i}{\sum_i w_i}$ (bold) and a description of the fit: "c_tmin-tmax" indicates a constant fit to the fit window $[t_{\min}, t_{\max}]$, "c_src" a constant plus an exponential at the source, "c_snk" a constant plus an exponential at the sink, and "c_src_snk" a constant plus an exponential at each of source and sink. The w-weighted average of the 30 highest probability fits is given by the blue band.
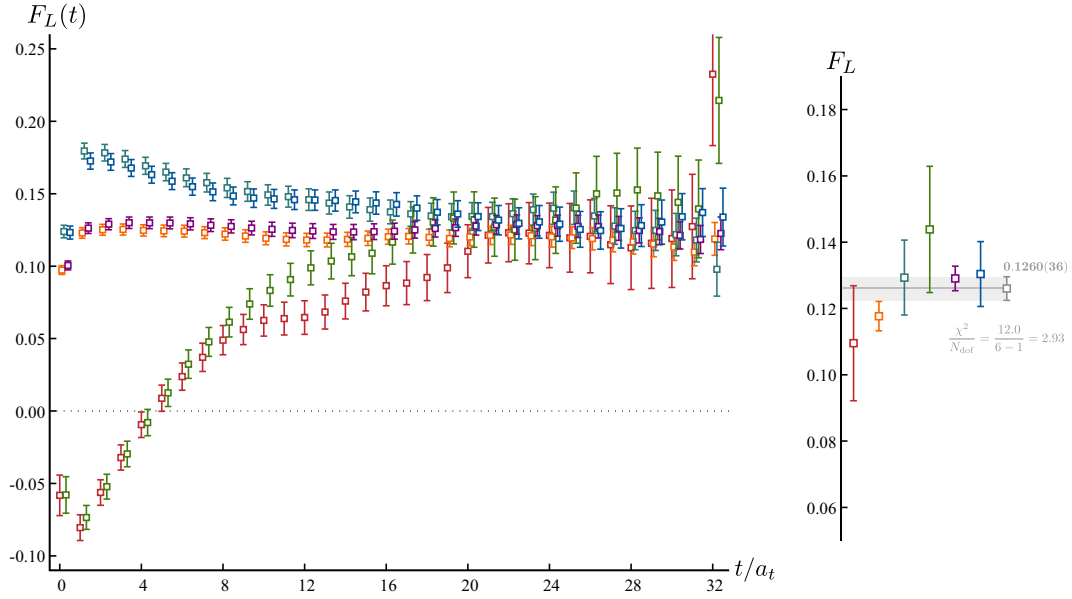
FIG. 21. An example of six $F_L(t)$ at the same $(Q^2, E_n^\star)$ corresponding to different momentum directions, irrep rows and current subductions. The left panel shows that they all likely plateau to the same constant value, but experience different amounts of excited-state pollution and have different signal/noise. The right panel shows the fitted F_L values for each (using the model averaging procedure) which are then fitted to a constant to yield a single F_L value to be used in later stages of the analysis.

APPENDIX E: GLOBAL FITTING

As discussed in the body of the paper, attempts to fit all 128 $(Q^2, E_n^\star)$ points using the simple inverse of the data correlation matrix in the χ^2 lead to solutions which lie significantly and systematically below the data. We propose that with only 348 configurations, we are not producing reliable estimates of the entire data correlation matrix, and opt to reduce the impact of this by eliminating the poorly estimated smaller eigenvalues. We reduce the size of the data space by eliminating the linear combinations of data corresponding to those eigenvectors of the data correlation matrix with eigenvalue smaller than λ_{cut}. When computing
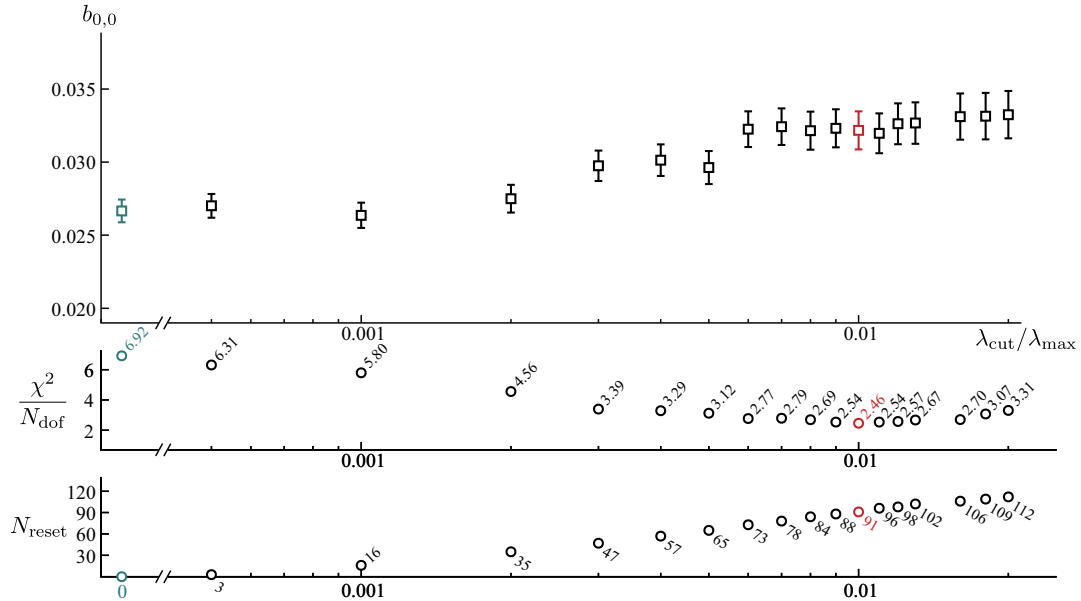

FIG. 22. The top panel shows the value of parameter $b_{0,0}$ in a "global fit" to 128 F points using Eq. (17), as a function of the cut used to reset eigenvalues of the data correlation. The middle and lower panels show the corresponding χ^2/N_{dof} and the number of reset eigenvalues. The blue points indicate the result of not resetting any eigenvalues, and the red points indicate the choice made for the global fits presented in Sec. VI B.

TABLE III. Variation with $F(Q^2, E^\star)$ parametrization and data range.

Fit form	Data	χ^2/N_{dof}	$f_R(0)$
exp_poly_100	All	$83/(128{-}91{-}4) = 2.5$	$0.1868(68) - i0.0095(9)$
z_poly_100	All	$81/(128{-}91{-}4) = 2.5$	$0.1862(67) - i0.0079(8)$
exp_poly_110	All	$82/(128{-}91{-}5) = 2.6$	$0.1887(75) - i0.0083(27)$
z_poly_110	All	$81/(128{-}91{-}5) = 2.5$	$0.1869(67) - i0.0070(13)$
exp_poly_100	Small Q^2	$115/(91{-}50{-}4) = 3.1$	$0.1852(67) - i0.0096(9)$
exp_poly_10	Small Q^2	$136/(91{-}50{-}3) = 3.6$	$0.1752(65) - i0.0089(8)$
z_poly_100	Small Q^2	$117/(91{-}50{-}4) = 3.2$	$0.1840(66) - i0.0082(7)$
z_poly_11	Small Q^2	$120/(91{-}50{-}4) = 3.2$	$0.1842(62) - i0.0049(13)$
exp_poly_000	Res. region	$75/(64{-}37{-}3) = 3.1$	$0.1869(63) - i0.0062(8)$
z_poly_000	Res. region	$75/(64{-}37{-}3) = 3.1$	$0.1852(62) - i0.0061(8)$

the χ^2/N_{dof} we reduce the number of degrees of freedom by the number of "reset" eigenvalues. Figure 22 shows the result of this procedure as a function of λ_{cut}, where we observe that for $\lambda_{\text{cut}} \gtrsim 0.006\lambda_{\text{max}}$, the value of the fit parameter $b_{0,0}$ plateaus, and the χ^2/N_{dof} varies rather little. We choose to use $\lambda_{\text{cut}} = 0.01\lambda_{\text{max}}$ as our default in the analysis presented in the paper, which happens to be the point at which the χ^2/N_{dof} takes its minimum value.

Using the data correlation matrix eigenvalue cut found above, we explore the variation in fits under changes in $F(Q^2, E^\star)$ parametrization, and $K\pi$ elastic scattering amplitude parametrization.

Table III illustrates a sample of $F(Q^2, E^\star)$ parametrization variations when the F_L data is corrected with KM$_g$. The amplitudes are given labels as follows: e.g., "exp_poly_110" indicates Eq. (15) where $f_{0,0}, f_{0,1}, a_{1,0}, a_{1,1}$, and $a_{2,0}$ are free parameters, and "z_poly_110" indicates Eq. (16) where $b_{0,0}, b_{0,1}, b_{1,0}, b_{1,1}$, and $b_{2,0}$ are free parameters. The data ranges are as follows: "all," indicating all 128 data points, "small Q^2" indicating only data with $a_t^2 Q^2 < 0.015$, and "res. region" indicating only data in the window $0.15 < a_t E^\star < 0.16$.

TABLE IV. Variation with $K\pi$ elastic scattering amplitude parametrization.

Amplitude	χ^2/N_{dof}	$f_R(0)$
BW$_a$	$102/(128{-}84{-}4) = 2.6$	$0.1918(63) - i0.0083(5)$
BW$_b$	$85/(128{-}90{-}4) = 2.5$	$0.1924(69) - i0.0084(6)$
BW$_c$	$93/(128{-}86{-}4) = 2.5$	$0.1937(65) - i0.0086(5)$
BW$_d$	$92/(128{-}85{-}4) = 2.4$	$0.1975(64) - i0.0089(5)$
BW$_e$	$91/(128{-}84{-}4) = 2.4$	$0.1940(64) - i0.0086(5)$
BW$_f$	$82/(128{-}89{-}4) = 2.3$	$0.1963(67) - i0.0087(6)$
KM$_g$	$81/(128{-}91{-}4) = 2.5$	$0.1862(67) - i0.0079(8)$
KM$_h$	$77/(128{-}96{-}4) = 2.7$	$0.1849(71) - i0.0075(19)$
KM$_i$	$84/(128{-}93{-}4) = 2.7$	$0.1857(67) - i0.0075(9)$
KM$_j$	$82/(128{-}91{-}4) = 2.5$	$0.1860(67) - i0.0080(7)$
KM$_k$	$83/(128{-}90{-}4) = 2.4$	$0.1895(66) - i0.0082(7)$
KM$_l$	$80/(128{-}91{-}4) = 2.4$	$0.1883(66) - i0.0080(8)$

Table IV illustrates variation using changes in $K\pi$ elastic scattering amplitude when the parametrization "z_poly_100" [Eq. (17)] is used. These variations, as well as the variations observed in "level-by-level" analysis are used to come to the conservative estimate presented in Eq. (18).

APPENDIX F: SIMPLISTIC EXTRAPOLATION TO PHYSICAL KINEMATICS

A phenomenologically motivated extrapolation to physical kinematics can be justified by the observation made in Fig. 4 of Ref. [17] that the reduced coupling appears to be largely quark mass independent. Taking this literally, the total hadronic width of the K^* would be

$$\Gamma_R = 3 \cdot \Gamma(K^+\pi^0) = 3 \cdot \frac{2}{3}\frac{k_{K\pi}^{\star 3}}{m_R^2}|\hat{c}_R|^2 = 42(3) \text{ MeV},$$

where the physical mass $m_R = 892$ MeV is used for the mass of the K^* in the kinematic quantities. This is in reasonable agreement with the PDG width [30].
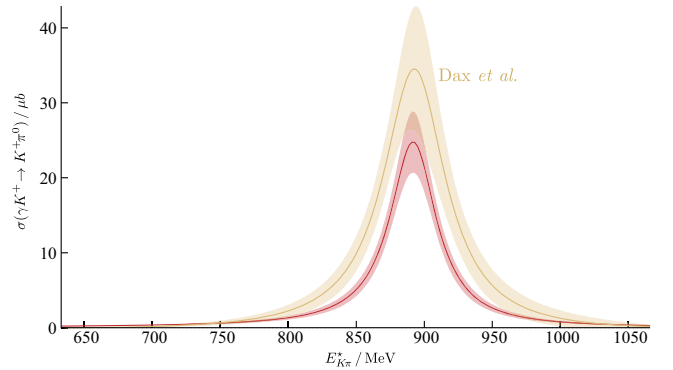

FIG. 23. Simplistic extrapolation of the cross section to physical light quark mass as described in the text. Compared to twice subtracted dispersion results of Dax et al. [5], with subtraction constants fixed by experimental radiative transition width and chiral anomaly (their Fig. 8).

It is not obvious how $f_R(0)$ should evolve with changing quark mass, but if we assume that it does not change, then we can make the following, rather crude, estimate of the radiative decay width,

$$\Gamma(K^{*+} \to K^+\gamma) = \frac{4}{3}\alpha \frac{k_{K\gamma}^{\star 3}}{m_K^2}|f_R(0)|^2 = 40(6) \text{ keV},$$

which is also in reasonable agreement with the PDG averaged partial width [30]. The agreement is slightly worse if $f_R(0)/m_K$ is assumed to be constant (as suggested by a simplistic extension of the argument presented in Ref. [31]), as then $\Gamma(K^{*+} \to K^+\gamma) = 37(5)$ keV.

The extrapolated hadronic width, and the (first) extrapolated radiative width can be used in a simplistic pole-only form for the cross section for physical kinematics,

$$\sigma(\gamma K^+ \to K^+\pi^0) = \frac{2\pi}{k_{K\gamma}^{\star 2}} \frac{m_R^2 \Gamma_R \Gamma(K^{*+} \to K^+\gamma)}{|(m_R - i\Gamma_R/2)^2 - s|^2},$$

using again the physical value of m_R in all kinematic quantities. Figure 23 shows this cross section estimate plotted along with the estimate given in Fig. 8 of Ref. [5] coming from a dispersive approach making use of the PDG radiative decay partial widths and the chiral anomaly to set the subtraction constants.

[1] W. C. Carithers, P. Muhlemann, D. Underwood, and D. G. Ryan, Phys. Rev. Lett. **35,** 349 (1975).
[2] D. Berg *et al.*, Phys. Lett. **98B,** 119 (1981).
[3] C. Chandlee *et al.*, Phys. Rev. Lett. **51,** 168 (1983).
[4] D. Carlsmith *et al.*, Phys. Rev. Lett. **56,** 18 (1986).
[5] M. Dax, D. Stamen, and B. Kubis, Eur. Phys. J. C **81,** 221 (2021).
[6] R. A. Briceno, J. J. Dudek, and R. D. Young, Rev. Mod. Phys. **90,** 025001 (2018).
[7] L. Lellouch and M. Luscher, Commun. Math. Phys. **219,** 31 (2001).
[8] R. A. Briceño, M. T. Hansen, and A. Walker-Loud, Phys. Rev. D **91,** 034501 (2015).
[9] R. A. Briceño and M. T. Hansen, Phys. Rev. D **92,** 074509 (2015).
[10] R. A. Briceno, J. J. Dudek, R. G. Edwards, C. J. Shultz, C. E. Thomas, and D. J. Wilson, Phys. Rev. Lett. **115,** 242001 (2015).
[11] R. A. Briceño, J. J. Dudek, R. G. Edwards, C. J. Shultz, C. E. Thomas, and D. J. Wilson, Phys. Rev. D **93,** 114508 (2016).
[12] C. Alexandrou, L. Leskovec, S. Meinel, J. Negele, S. Paul, M. Petschlies, A. Pochinsky, G. Rendon, and S. Syritsyn, Phys. Rev. D **98,** 074502 (2018).
[13] L. Leskovec and S. Prelovsek, Phys. Rev. D **85,** 114507 (2012).
[14] C. J. Shultz, J. J. Dudek, and R. G. Edwards, Phys. Rev. D **91,** 114501 (2015).
[15] R. G. Edwards, B. Joo, and H.-W. Lin, Phys. Rev. D **78,** 054501 (2008).
[16] H.-W. Lin *et al.* (Hadron Spectrum Collaboration), Phys. Rev. D **79,** 034502 (2009).
[17] D. J. Wilson, R. A. Briceno, J. J. Dudek, R. G. Edwards, and C. E. Thomas, Phys. Rev. Lett. **123,** 042002 (2019).
[18] M. Peardon, J. Bulava, J. Foley, C. Morningstar, J. Dudek, R. G. Edwards, B. Joo, H.-W. Lin, D. G. Richards, and K. J. Juge (Hadron Spectrum Collaboration), Phys. Rev. D **80,** 054506 (2009).

[19] R. Omnes, Nuovo Cimento **8,** 316 (1958).
[20] C. E. Thomas, R. G. Edwards, and J. J. Dudek, Phys. Rev. D **85,** 014507 (2012).
[21] R. A. Briceño, J. J. Dudek, and L. Leskovec, Phys. Rev. D **104,** 054509 (2021).
[22] J. J. Dudek, R. G. Edwards, and C. E. Thomas (Hadron Spectrum), Phys. Rev. D **87,** 034505 (2013); **90,** 099902(E) (2014).
[23] J. J. Dudek, R. G. Edwards, and C. E. Thomas, Phys. Rev. D **86,** 034031 (2012).
[24] C. B. Lang, L. Leskovec, D. Mohler, and S. Prelovsek, Phys. Rev. D **86,** 054508 (2012).
[25] S. Prelovsek, L. Leskovec, C. B. Lang, and D. Mohler, Phys. Rev. D **88,** 054508 (2013).
[26] G. S. Bali, S. Collins, A. Cox, G. Donald, M. Göckeler, C. B. Lang, and A. Schäfer (RQCD Collaboration), Phys. Rev. D **93,** 054509 (2016).
[27] R. Brett, J. Bulava, J. Fallica, A. Hanlon, B. Hörz, and C. Morningstar, Nucl. Phys. **B932,** 29 (2018).
[28] W. I. Jay and E. T. Neil, Phys. Rev. D **103,** 114502 (2021).
[29] C. G. Boyd, B. Grinstein, and R. F. Lebed, Phys. Rev. Lett. **74,** 4603 (1995).
[30] R. L. Workman (Particle Data Group), Prog. Theor. Exp. Phys. **2022,** 083C01 (2022).
[31] M. Niehus, M. Hoferichter, and B. Kubis, J. High Energy Phys. 12 (2021) 038.
[32] R. R. Horgan, Z. Liu, S. Meinel, and M. Wingate, Phys. Rev. D **89,** 094501 (2014).
[33] R. G. Edwards and B. Joo (SciDAC, LHPC, UKQCD Collaborations), Nucl. Phys. B, Proc. Suppl. **140,** 832 (2005).
[34] M. A. Clark, R. Babich, K. Barros, R. C. Brower, and C. Rebbi, Comput. Phys. Commun. **181,** 1517 (2010).
[35] R. Babich, M. A. Clark, and B. Joo, in *Proceedings of the SC 10 (Supercomputing 2010) New Orleans, Louisiana, 2010* (2010), arXiv:1011.0024.

[36] K. Clark, B. Joo, A. Strelchenko, M. Cheng, A. Gambhir, and R. Brower, in *Proceedings of SC 16 (Supercomputing 2016) Salt Lake City, Utah, 2016* (2016).

[37] B. Joó, D. Kalamkar, K. Vaidyanathan, M. Smelyanskiy, K. Pamnany, V. Lee, P. Dubey, and W. Watson, in *Supercomputing*, Lecture Notes in Computer Science Vol. 7905, edited by J. Kunkel, T. Ludwig, and H. Meuer (Springer Berlin Heidelberg, 2013), pp. 40–54.

[38] B. Joó, MG_PROTO: A Multigrid Library for QCD, https://github.com/JeffersonLab/mg_proto/.

[39] J. C. Osborn, R. Babich, J. Brannick, R. C. Brower, M. A. Clark, S. D. Cohen, and C. Rebbi, Proc. Sci., LATTICE2010 (**2010**) 037 [arXiv:1011.2775].

[40] R. Babich, J. Brannick, R. C. Brower, M. A. Clark, T. A. Manteuffel, S. F. McCormick, J. C. Osborn, and C. Rebbi, Phys. Rev. Lett. **105**, 201602 (2010).

[41] J. J. Dudek, R. G. Edwards, P. Guo, and C. E. Thomas (Hadron Spectrum Collaboration), Phys. Rev. D **88**, 094505 (2013).